Design of a Vertical Take-Off and Landing Aerial Vehicle with Retractable Wings

Corentin Barut, Davide Mazzola, Rémy Grange, Romain Lattion
Ecole Polytechnique Fédérale de Lausanne (EPFL)
Collaboration with EPFL Xplore

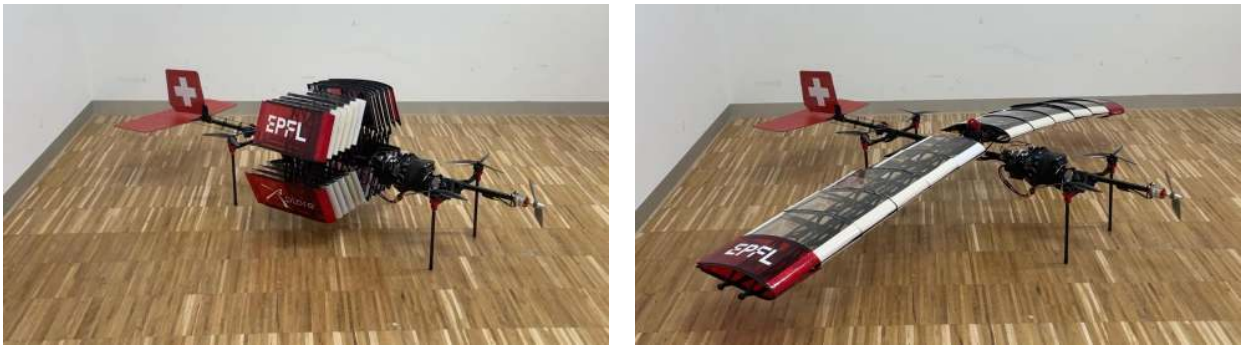

Fig. 1: Comparison of the folded (left) and deployed (right) states of the prototype.

***Abstract*—This work presents the design and experimental investigation of a vertical take-off and landing (VTOL) unmanned aerial vehicle (UAV) incorporating a retractable wing concept. The proposed architecture aims to combine multirotor hover capability with the aerodynamic efficiency of fixed-wing flight while addressing stringent volumetric constraints. A scissor-based deployment mechanism was selected to achieve a high wing retraction ratio while preserving a continuous aerodynamic profile in the deployed configuration.**

The project focuses on system-level integration, including mechanical design, structural dimensioning, propulsion sizing, and flight control implementation based on a Pixhawk–PX4 architecture. Aerodynamic analyses were conducted using two-dimensional and three-dimensional CFD simulations to support wing dimensioning and assess finite-wing effects. Aerodynamic stability analyses were also conducted in order to analyze the static and dynamic stability of the VTOL aircraft. These numerical investigations were complemented by experimental tests performed at the WindShape facility at EPFL to evaluate lift generation and flap effectiveness.

Several prototype iterations were developed and flight-tested. While stable fixed-wing flight was successfully demonstrated, a fully autonomous VTOL sequence could not be achieved within the project timeframe due to limitations related to mass increase, propulsion capability, control surface sizing, and aeroelastic effects. Nevertheless, the retractable wing mechanism proved mechanically robust and aerodynamically viable, providing a solid basis for future developments

I. Introduction

VERTICAL take-off and landing (VTOL) unmanned aerial vehicles (UAV) combine the hovering capabilities of multirotor platforms with the aerodynamic efficiency of fixed-wing aircraft. This hybrid approach enables operation in confined environments while maintaining extended range and endurance during forward flight.

The authors are with EPFL Xplore, Ecole Polytechnique Fédérale de Lausanne (EPFL), CH1015 Lausanne, Switzerland.

This project focuses on the design and prototyping of a VTOL aircraft featuring retractable wings. The proposed concept relies on a fixed propulsion layout combined with a mechanical wing deployment mechanism. With the wings folded, the vehicle operates in hover mode with a reduced footprint, enabling precise maneuvering and safe operation in restricted spaces. Once sufficient clearance is available, the wings can be deployed, allowing the drone to transition to forward flight and benefit from increased aerodynamic efficiency.

The primary objective of this project is to develop and validate a functional VTOL prototype that integrates mechanical design, electronics and flight control within a single coherent system. The emphasis is placed on system integration, robustness, and experimental validation rather than on exhaustive aerodynamic or control optimization. The design process encompasses the development of a mechanical structure, a retractable wing deployment mechanism, a centralized power and electronics architecture, and the configuration and tuning of a PX4-based flight control system.

The prototype was developed in collaboration with EPFL Xplore, within the broader context of space robotics and autonomous exploration systems. The retractable-wing architecture enables a compact folded configuration, reducing the required volume during launch and making the system compatible with space-constrained environments such as launch vehicles. Once deployed, the rigid wings provide structural support for potential integration of solar panels, enabling extended autonomy. The VTOL capability allows both precise localized exploration and efficient long-distance traversal, which are key requirements for robotic exploration missions on planetary bodies such as Mars, the Moon, or other low-atmosphere or low-gravity environments. While the present work focuses on terrestrial validation as a proof of concept, the proposed architecture is intended as a scalable platform

for future extraterrestrial applications.

II. Related Work

Deployable and foldable wing concepts have been explored in VTOL UAVs to enhance compactness during hover and take-off and landing in confined spaces, while enabling efficient fixed-wing cruise flight. A broad classification of morphing wings, including folding mechanisms, is provided by Min et al., who discuss trade-offs in structural complexity, weight, and aerodynamic gains for variable-geometry aircraft [1].

More recent studies have explored advanced morphing architectures, including telescopic and rotating wing concepts, aimed at improving adaptability across different flight configurations while maintaining compact storage capabilities. Such designs are particularly attractive for systems constrained by volume, as they enable span variation while preserving a fixed propulsion layout [2].

However, conventional telescopic wings rely on nested structural sections that slide into one another along the span. This structural constraint inherently limits the achievable retraction ratio and leads to a stepped internal geometry, since outer wing sections must fit within inner ones. As a result, maintaining a continuous aerodynamic profile along the entire wingspan remains challenging in telescopic morphing configurations.

Dedicated investigations into telescopic wing aircraft, such as the work by Zhao and Hu, have demonstrated that spanwise extension can significantly alter lift and drag characteristics, enabling a single platform to satisfy multiple flight requirements [3]. While these results confirm the aerodynamic potential of telescopic mechanisms, the associated geometric discontinuities and limited retraction factors restrict their applicability for highly compact aerial systems.

In contrast, the present work introduces a scissor-type retractable wing mechanism for a fixed-propulsion VTOL drone. This enables a high retraction factor and compact hover configuration without nested boxes, while maintaining a continuous airfoil profile when fully deployed.Such a configuration is particularly relevant for compact VTOL UAVs, where both volumetric constraints and aerodynamic efficiency are critical. To the authors' knowledge, no existing VTOL platform uses a scissor-based retractable wing. This positions the present design as a distinct alternative to conventional folding or telescopic wing solutions for compact aerial systems operating under strong volumetric constraints.

III. System Overview

A. General Overview

The main objective of this project is to design and build a VTOL drone prototype capable of retracting and deploying its wings depending on the current flight mode. The retracted-wing configuration is used during hover flight in order to reduce the overall footprint of the vehicle, allowing precise maneuvering in confined or cluttered environments. Once the drone reaches an open area, the user can deploy the wings through a simple command. The drone then accelerates in the horizontal direction and once sufficient airspeed is achieved, the rotational speed of the hover propellers is progressively reduced. This process enables a smooth and continuous transition from hover mode to fixed-wing (airplane) flight. The transition back to hover mode follows the reverse sequence. First, the four hover propellers are reactivated while the drone pitches backward to decelerate. Once the vehicle has fully recovered its hover configuration, the wings can be retracted, allowing the drone to perform precise maneuvers close to the target location or landing zone.

To meet these requirements, the drone is composed of several structural and functional subsystems. The following element numbers are referring to Fig. 2, which shows an exploded view of the system. The entire assembly is built around a central square-section carbon fiber tube with dimensions of 10×10 mm and a wall thickness of 1 mm.

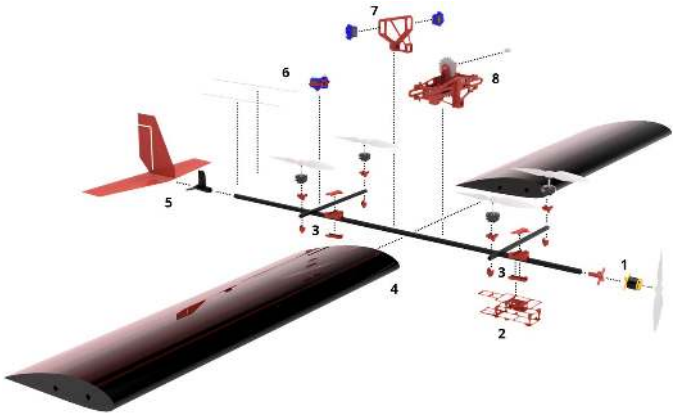

Fig. 2: Exploded view of the prototype.

The main propulsion motor (1) is mounted at the front of the structure. The hover propellers (3) are mounted perpendicular to the central tube on a braided carbon fiber tube with a square section of 8×8 mm and a wall thickness of 1 mm. The onboard electronics and battery (2) are strategically positioned to ensure that the center of mass is located at the intersection of the diagonals formed by the rectangle defined by the hover propellers. Since the drone undergoes a flight mode transition, this center of mass must also be ahead of the aerodynamic center of the wings (4). Wing deployment (8) is actuated by a 12 V DC motor coupled to a 3D-printed lead screw mechanism with an inverted thread, converting the motor's rotational motion into linear translation. The wing flaps are directly actuated by dedicated servo motors (7). The rear section of the drone is dedicated to the empennage (5), as well as the actuation system (6) for the control surfaces used during airplane mode flight.

The main physical and performance characteristics achieved with this prototype are summarized in Table I.

TABLE I: Physical characteristics of the prototype

Property	Value
Total length	1.2 m
Wingspan (deployed)	1.57 m
Width (wings folded)	0.29 m
Total mass	2.6 kg
Front motor power	380 W
Chord	250 mm
Airfoil profile	NACA 4418
Deployment time	10 s
Folding time	12 s

B. Electronics and Components

The electronic system is powered by a single onboard battery directly connected to a PM07 power module, which acts as the central power distribution unit. The PM07 supplies regulated power to the Pixhawk flight controller and distributes high-current power to the propulsion systems. Both the 60A 4-in-1 Electronic Speed Controller (ESC) used for the hover motors and the dedicated 40A ESC driving the forward propulsion motor are directly connected to the power module.

Power distribution within the system is based on a simple and robust dual-voltage architecture. A regulated 5 V rail is provided by the Battery Elimination Circuit (BEC) integrated in the forward propulsion ESC and is used to supply all low-voltage components, including the servos, receiver, sensors, and auxiliary electronics. This 5 V rail is routed through the PM07 power module, allowing all servo actuators to be connected to a common regulated supply. In addition, a dedicated external BEC is used to provide a stabilized 12 V supply for the DC motor responsible for wing deployment. The remaining power management functions, including voltage regulation and current sensing, are handled directly by the power module.

The energy storage system is based on a 4S lithium-polymer battery, selected as a compromise between power density, weight, and compatibility with the selected motors and ESCs. This configuration provides sufficient voltage headroom for both hover and forward propulsion, while maintaining acceptable current levels for the power electronics. Since hover operation represents the most power-intensive flight regime, overall endurance is mainly limited by the cumulative duration of vertical flight and transition phases rather than cruise operation.

Motor control signals are distributed from the Pixhawk through individual output ports of the power module, each corresponding to a dedicated motor or actuator control line. This architecture allows clean separation between power delivery and control signals, while maintaining compatibility with standard Pixhawk wiring and configuration practices.

Propeller selection was driven by both aerodynamic efficiency and integration constraints. The maximum allowable propeller diameter for the forward propulsion system is limited by the width of the drone with the wings folded, resulting in an upper bound of approximately 13 inches. Experimental tests were conducted using smaller propellers within this constraint, with a typical configuration around 10 inches diameter and 4 inches pitch.

For the hover propulsion system, two-bladed propellers were selected instead of three-bladed alternatives in order to minimize parasitic drag during airplane mode flight. Comparative tests using thrust estimation tools and experimental data showed that, for equivalent diameter and pitch, two-bladed propellers provide approximately 8% higher thrust efficiency than three-bladed propellers, while also reducing aerodynamic drag when the motors are unpowered during forward flight.

The Pixhawk flight controller is responsible for vehicle stabilization, navigation and flight mode management. Standard connections between the Pixhawk and the PM07 power module are implemented. A FrSky RX8R receiver operating at 2.4 GHz is used for radio control and provides up to 16 independent channels, enabling simultaneous control of propulsion, wing deployment, flight modes and safety-related functions. Fig. 3 summarizes the overall electronic architecture and illustrates the interaction between the main components, including the power module, flight controller, propulsion systems and auxiliary control electronics.

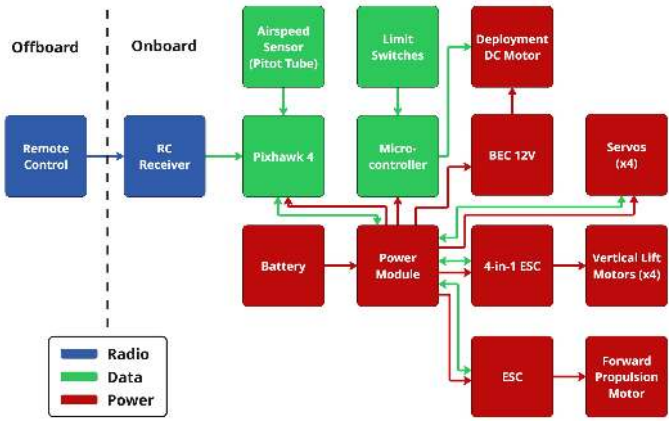

Fig. 3: Primary electronic components.

Wing deployment is actuated by a Micro Metal Gearmotor N20 (12V, 100RPM, 298:1 reduction ratio) controlled by an auxiliary microcontroller interfaced with the RC receiver. 12 V tension is furnished by the 12 V BEC but further tests were conducted under a controlled over-voltage of 16.5 V to increase deployment speed while remaining within acceptable thermal limits, resulting in a full deployment time of $t = 10\,\text{s}$.

Electrical analysis indicates a mean current draw of $I_{avg} \approx 0.13\,\text{A}$, yielding an average power consumption of:

$$P = U \times I_{avg} = 16.5 \times 0.13 = 2.15\,\text{W} \tag{1}$$

The total energy required for a single deployment cycle is $E = 21.5\,\text{J}$. Mechanically, the system operates with a high safety margin; the estimated load torque is $0.22\,\text{kg}\cdot\text{cm}$ ($0.022\,\text{N}\cdot\text{m}$), which utilizes only $\approx 8\%$ of the motor's stall torque ($2.9\,\text{kg}\cdot\text{cm}$).

The dedicated extra microcontroller manages the deployment mechanism, including the DC motor and the limit switches used to detect the fully deployed and folded positions. However, this architecture introduces the challenge that the Pixhawk does not inherently know the current state of the wings (folded, deployed, or in transition). This limitation was deemed acceptable for the present prototype, as wing

deployment is commanded manually and visually monitored during testing.

The sizing of the propulsion system, power electronics and energy storage was initially performed during the early stages of the project, based on preliminary estimates of vehicle mass, wing geometry, and target cruise speed. As the project progressed, several key parameters evolved, including total mass, wingspan, chord length and airfoil selection. As a result, the final configuration does not represent a fully optimized design for the current prototype, but rather a functional compromise enabling reliable testing of all flight modes. Further optimization of motor selection, propeller geometry and battery capacity could be achieved in future iterations once the final airframe geometry and mass distribution are fixed.

C. Drone Structure

The entire drone relies on a main structural element acting as a central spine. All components necessary for the drone's operation and performance are mounted along this main axis. As described earlier, the primary structural element consists of a 1000 mm long carbon fiber tube with a square cross-section of 10 × 10 mm and a wall thickness of 1 mm, resulting in a total mass of 55 g. This solution is significantly lighter than an equivalent aluminum tube, which would weight approximately 98 g for the same dimensions. The primary design objective of this structural concept is to minimize mass while maintaining sufficient stiffness and structural integrity, which is critical for flight efficiency and overall system performance.

This section describes the different components mounted on the main axis, starting from the front of the UAV based on the exploded view in Fig. 2.

1) Main Propulsion Motor Fixation: At the front of the structure (element (1) in Fig. 2), the propulsion motor is mounted using a rigid 3D-printed polyethylene terephthalate glycol-modified (PETG) support specifically designed to interface with the main carbon fiber tube. A detailed view of this fixation system is shown in Fig. 4, where the two constitutive parts are identified as element (1) and element (2).

The fixation mechanism consists of two interlocking components. A screw passes through the cylindrical bore of each element, while a nut is housed inside the hexagonal cavity of element (2). When the screw is tightened, the conical part is progressively pulled into its corresponding negative geometry within the other one. This relative motion induces a radial expansion of element (1), which presses against the inner wall of the carbon fiber tube. As a result, the assembly behaves as an internal expansion anchor, generating controlled radial pressure that ensures a secure and vibration-resistant attachment of the propulsion motor. This solution enables the motor mount to be fixed using a single screw, thereby minimizing fastener count and contributing to the overall lightweight design of the structure.

2) Hover Propulsion System: Transversal Tubes and Motor Fixation: The second structural element mounted on the main axis consists of a transversal carbon fiber tube with a square cross-section of 8 × 8 mm, a wall thickness of 1 mm, and a length of 250 mm. A quadcopter brushless motor is mounted

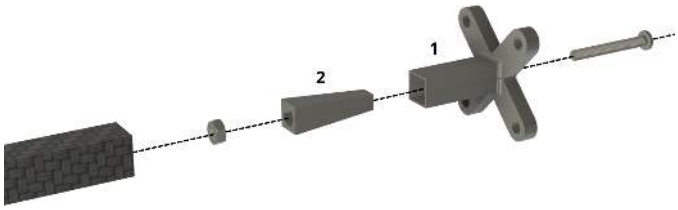

Fig. 4: 3D printed PETG support of the main engine to the carbon tube

at each end of this tube, forming the lateral propulsion system used during hover flight. The connection between the main structural spine (10 × 10 mm carbon fiber tube) and the transversal propulsion tubes is ensured by a custom-designed 3D-printed carbon fiber–reinforced polyethylene terephthalate (PET-CF) mounting bracket (See Fig. 5a). This component serves as the mechanical interface between the two different tube geometries and plays a critical role in maintaining structural alignment and load transfer between the hover propulsion system and the main frame. During the early stages of the design, cylindrical carbon fiber tubes were initially considered for both the longitudinal and transversal structural elements. However, experimental evaluations revealed insufficient resistance to torsional loads at the interface with the PETG mounting bracket. Under operational conditions, the cylindrical tubes exhibited radial vibrations and relative rotation within the printed part, indicating inadequate grip and torque transmission. To address this issue, the structural elements were redesigned using square-section carbon fiber tubes. The flat contact surfaces provided by the rectangular geometry significantly improve mechanical interlocking with the PETG bracket, resulting in enhanced torsional stiffness and a noticeable reduction in vibration. The mounting bracket clamps both the longitudinal and transversal carbon fiber tubes and is secured using two screws and two nuts, forming a rigid yet lightweight assembly.

The length of the transversal tube was determined by the maximum allowable width imposed by the folded-wing configuration. This folded wingspan was intentionally selected as the limiting dimension for the overall vehicle width. Since one of the primary objectives of the drone design is to significantly reduce its span in hover mode, allowing operation in confined environments, it would be counterproductive for the hover propellers to extend beyond the width of the folded wings. Consequently, the propeller-to-propeller distance was constrained to remain within this envelope.

Each quadcopter motor is mounted using four screws, two of which fulfill a dual function. These screws simultaneously secure the motor to a secondary 3D-printed PETG mounting piece and fasten this PETG component directly to the transversal carbon fiber tube. By assigning both functions to the same fasteners, the need for additional, redundant screws dedicated solely to motor-to-mount fixation is eliminated. This approach reduces the total number of fasteners, contributing to mass reduction, simplified assembly, and improved structural efficiency, while maintaining a rigid and reliable

motor attachment (See Fig. 5b). Moreover, this 3D-printed part includes a support for a carbon fiber tube, which helps maintain structural integrity during takeoff and landing when contacting the ground (See Fig. 1).

An identical transversal tube and mounting assembly is also installed downstream of the wing mechanism, as illustrated in Fig. 2, ensuring symmetry and a balanced thrust distribution during vertical flight.

(a) Fixation of transversal tube

(b) Fixation of a hover engine

Fig. 5: Fixations to support the engines of the quadcopter

3) Electronics Support and Integration: Immediately downstream of the first transversal bar supporting the quadcopter motors, a custom-designed 3D-printed PETG structure is integrated to support the onboard electronics (see Fig. 2, element (2)). This component is mounted directly onto the main carbon fiber spine and serves as the primary mechanical interface for the electronics.

As with all structural components of the drone, mass reduction was a primary design objective. For this reason, the electronics support was extensively lightened through the introduction of internal cut-outs and through-holes, as illustrated in Fig. 6. These openings significantly reduce material usage while maintaining sufficient structural rigidity for the supported components. The electronics support is fixed to the main carbon fiber tube using only two screws and two nuts. To ensure adequate mechanical stability despite the reduced number of fasteners, the screws are intentionally mounted at an inclined angle with respect to the tube axis. This configuration improves resistance to both axial sliding and rotational motion by introducing a combined normal and shear force component at the interface. Compared to two purely vertical screws, which would primarily resist separation in a single direction, the inclined fasteners provide improved clamping efficiency and torsional stiffness, thereby reducing the risk of relative motion and vibration under dynamic flight loads. In addition to mass reduction, the through-holes serve a second critical function related to cable management. The openings allow cables to pass directly through the structure and be guided along the main carbon fiber spine, where they are secured. As a result, no cables protrude laterally from the electronics support; instead, all connections exit from the top of the enclosure and are routed directly to their respective electronic components. This approach improves mechanical robustness, reduces the risk of cable entanglement, and results in a cleaner and more maintainable assembly. The third function of the openings concerns thermal management. Several onboard electronic components generate significant heat during operation, most notably the power distribution board highlighted in the zoomed view shown in Fig. 6 (red circle). The perforated structure allows air to circulate through the electronics support, promoting passive convective cooling. To further enhance airflow, the power board is mounted on spacer pins, ensuring that it does not come into direct contact with the PETG enclosure. This spacing creates an air gap beneath the board, enabling airflow on both sides and improving heat dissipation during operation. To facilitate fabrication, the components are 3D-printed as separate parts and subsequently assembled using four screws and four metallic threaded inserts.

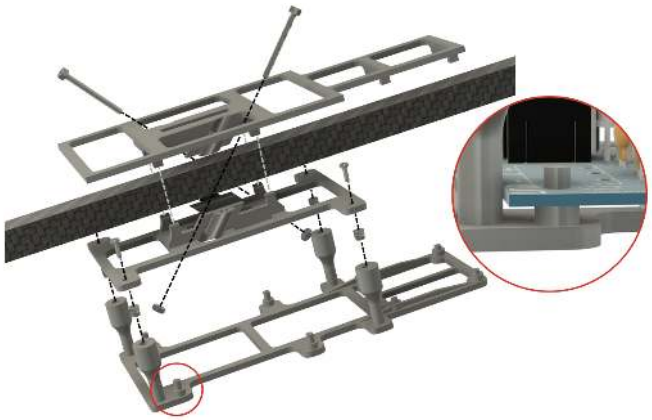

Fig. 6: 3D printed PETG support for the electronic components

4) Wing Flap Servo Fixation: Continuing along the main carbon fiber spine toward the rear of the drone, the next structural element is the support for the servo motors actuating the wing flaps, identified as element (7) in Fig. 2. These servo motors are responsible for controlling the control surfaces during fixed-wing flight. The servos are mounted on a custom-designed 3D-printed PETG support, using two nylon screws per servo and two nuts, as shown in Fig. 7. A distinctive feature of this support is that it is not fastened to the main carbon fiber tube using screws. Instead, the PETG component is designed to slide axially along the carbon tube during assembly. As a result, this element must be installed first on the main structural spine, prior to the mounting of the other structural components that are rigidly fixed to the tube.

5) Rudder and Elevator Servo Fixation and Transmission: Continuing toward the rear of the drone along the main carbon fiber spine, the next structural elements are the servo motors actuating the rudder and elevator control surfaces, identified as element (6) in Fig. 2. These actuators provide the necessary

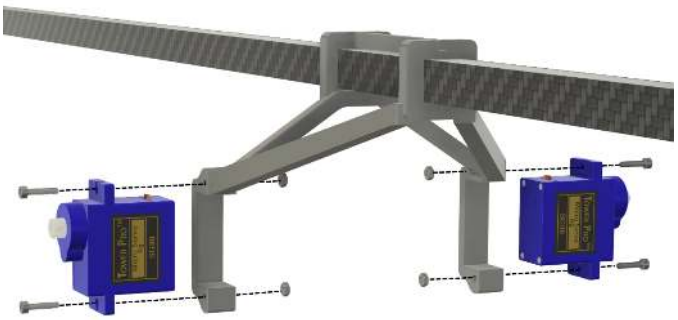

Fig. 7: 3D printed PETG support for the servo actioning the wing's flaps.

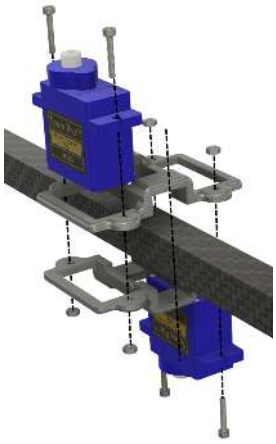

(a) Two parts PETG fixation for the motors

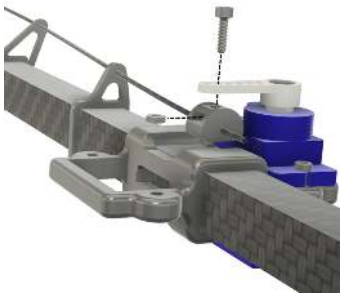

(b) Fixation of the carbon pushrod to the engine

Fig. 8: Fixation of servo motors and transmission mechanism responsible for controlling the elevator and the rudder.

control authority for attitude stabilization and maneuvering during flight.

The servo motors are mounted to the main carbon fiber tube using a custom-designed 3D-printed PETG support, shown in Fig. 8a. One servo is dedicated to actuating the elevator, while the second servo actuates the rudder. To minimize the occupied volume and avoid mechanical interference between the servo arms, the two servos are mounted upside down with respect to each other. This mirrored configuration allows both actuators to be placed in close proximity while ensuring that their respective servo arms do not collide during operation. The PETG support was designed to minimize material usage and fastener count while maintaining sufficient structural stiffness. The assembly is secured using two nylon screws and two nuts, forming a compact and lightweight attachment. Each servo is fixed to the PETG support at two dedicated attachment points. Notably, the same screws and nuts used to attach the servos are also used to clamp the two halves of the PETG support around the carbon fiber tube. This dual-purpose fastening strategy reduces part count and mass while providing adequate clamping force.

Figure 8b illustrates the mechanical transmission system responsible for conveying the rotational motion of the servo arm to the rudder. For clarity, only the transmission associated with the rudder servo is shown in this figure; the second servo has been intentionally removed to better expose the geometry and design of the linkage mechanism. The transmission system consists of a carbon fiber pushrod that transfers actuation from the servo arm to the control surface. To ensure correct kinematic behavior, the pushrod must undergo purely linear displacement. This requires the attachment point at the servo arm to be free to rotate about its axis, allowing the rotational motion of the servo arm to be converted into linear motion of the pushrod without introducing parasitic loads. To satisfy this requirement, a dedicated 3D-printed PETG linkage component was developed. This part incorporates an internal cavity that houses a bolt passing through the servo arm hole. The carbon fiber pushrod is clamped against the PETG component using a screw, which constrains the pushrod translationally while leaving the rotational degree of freedom unconstrained. As a result, the attachment through the screw can rotate freely around the servo arm hole, ensuring that the pushrod motion remains strictly linear throughout the servo actuation range.

6) Tail Fixation and Control Surface Linkage: The final structural element mounted on the main carbon fiber spine is located at the tail of the drone and supports the rudder and elevator assembly as illustrated in Fig. 2, element (5). Both control surfaces are bonded to a 3D-printed PETG tail support, which is itself bonded directly to the main carbon fiber tube.

This component is the only element of the structure that is permanently glued to the main spine. Adhesive bonding was selected in this case because the tail assembly does not need to be removed or repositioned during assembly or maintenance. In contrast, all components located forward of this element must be slid along the main tube during assembly, which would not be compatible with a permanently bonded joint. Since the tail support is installed last and does not interfere with the mounting sequence of other components, the use of adhesive bonding is both practical and structurally appropriate. In addition to adhesive bonding, the tail support is also mechanically secured using a cable tie wrapped around the PETG part and the carbon fiber tube. This secondary fastening provides an additional level of safety by preventing relative motion during operation. The combination of adhesive bonding and auxiliary mechanical retention ensures a robust, simple and lightweight design.

Figure 9b illustrates the fixation of the pushrod to the rudder. For clarity, only the rudder mechanism is shown; however, the same principle is applied identically to the elevator. The attachment consists of a two-part 3D-printed PETG assembly bonded directly to the movable control surface. The first part is permanently glued to the rudder (or elevator), forming a rigid base. The second part is clipped into the first, while remaining free to rotate about a defined axis, indicated by the dashed gray line in the figure. This second component incorporates a through-hole into which the carbon fiber pushrod is inserted as indicated by the light gray arrow in Fig. 9b and glued. The rotational freedom of this intermediate part allows the pushrod attachment to pivot about its axis, accommodating the angular motion of the control surface. This design ensures

that the pushrod experiences purely linear displacement, preventing bending stresses or parasitic loads during actuation. By decoupling rotational and translational degrees of freedom at the control surface interface, this solution guarantees precise transmission of servo commands to the rudder and elevator.

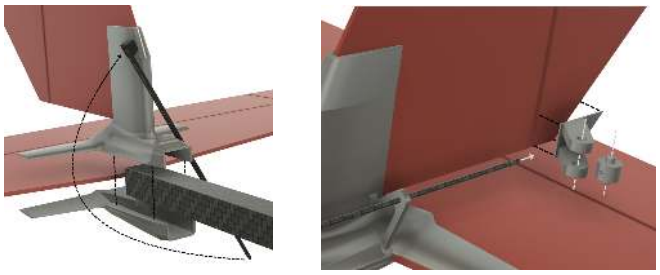

(a) Fixation of the tail and rudder to the main axile

(b) Fixation of pushrod to the rudder

Fig. 9: Fixation of the tail and rudder and link to the meachanical system for the activation of the control surface.

Table II summarizes the masses of all structural elements mounted on the main carbon fiber tube. The reported values include the corresponding screws and bolts and represent the total mass contribution of each component. This breakdown provides insight into the mass distribution along the primary structural axis and highlights the impact of the different fixation and support elements on the overall weight of the drone.

TABLE II: Masses of the structural elements mounted on the main carbon fiber tube (including screws and bolts).

Element	Mass [g]
Main propulsion motor fixation	6.3
Hover propulsion system:	
Transversal carbon tubes fixation (2 items)	40.2
Motor fixations (4 items)	43.2
Electronics support	29.0
Wing flap servo fixation	13.2
Rudder and elevator servo fixation	6.5
Rudder and elevator servo transmission	0.5
Guiders (4 items)	1.6
Tail fixation	14.4
Control surface linkage	0.9
Total	**156.8**

Table III presents the mass contribution of all carbon fiber components used in the structure of the drone. The reported values correspond to the total mass of each carbon element, taking into account multiple identical components where applicable. This breakdown highlights the relative contribution of the primary structural elements to the overall mass of the airframe.

TABLE III: Masses of the carbon fiber structural elements.

Carbon element	Mass [g]
Pushrods (2 items)	0.6
Main structural tube (10 × 10 mm, 1000 mm)	55.0
Transversal tubes (8 × 8 mm, 250 mm, 2 items)	21.0
Landing support tube (8 mm diameter, 200mm, 4 itmes)	26.8
Total	**103.4**

D. Wings

TABLE IV: Wing mechanism nomenclature

Term	Definition
Wing Cell	Discrete structural segment of the wing, comprising the upper and lower surface.
Scissor Linkage, linkage, link	Deployable pantograph mechanism connecting the wing cells and transmitting motion.
Deployment Slider	Interface component guiding wing deployment and transferring loads to the fuselage.
Drive Nut	Threaded component translating along the lead screw to convert rotation into linear motion.
Nesting	Mechanical capability of wing cells to interlock when retracted, maximizing compactness.

1) Folding Wing Concepts: Fabric vs. Rigid Cells: With the objective of designing a wing with a high retraction ratio, two distinct systems were investigated. The first approach consists of a structure composed of cells and a flexible fabric (see Fig. 1a). This mechanism allows for a significant folding ratio while remaining lightweight. Fabric-based wings are well-established and optimized technologies (e.g., paragliders), providing a robust developmental baseline. However, this system presents two major drawbacks. The first is structural rigidity; the internal framework must remain thin to avoid mechanical interference or damage to the fabric during deployment and retraction. To address this, a flat scissor-linkage system combined with a telescopic rod was considered. Nevertheless, such linkages exhibit low stiffness in the horizontal plane due to a reduced second moment of area. Furthermore, the joints are subject to high tensile loads, increasing friction and the risk of mechanical binding. The second issue involves aerodynamic profile stability. Due to fabric elasticity and pressure differentials during flight, the wing geometry deforms between the rigid cells, significantly degrading performance. While increasing internal pressure via an open leading edge, similar to a ram-air airfoil, can mitigate this, it inherently limits the aircraft's efficiency. For instance, paragliders rarely exceed a glide ratio of 10, whereas rigid-wing aircraft can achieve ratios exceeding 60 [4].

Consequently, a second system utilizing rigid cells was evaluated (see Fig. 10b). In this configuration, the wing is divided into a series of rigid cells, each split at the chord level. This design offers greater internal volume for the retraction mechanism and maintains a precise aerodynamic profile across the entire span. The primary trade-offs for this system include increased structural mass, as the number of required rigid profiles is doubled (two per cell). Additionally, the intersection zones between cells are critical; any discontinuities can trigger airflow disturbances, necessitating extremely tight tolerances and precise closure of the assembly.

(a) Fabric wing demonstration prototype

(b) Rigid wing demonstration prototype

Fig. 10: Comparison of the two developed wing folding prototypes.

2) Rigid Wing Design: Trade-offs between Rigidity, Mass, and Retraction Ratio: The wing structure consists of a series of cells split into two sections (upper and lower surfaces) along the chord. These cells are interconnected by a scissor linkage system, which provides structural rigidity and transmits the deployment and retraction motion. Two distinct linkage architectures were evaluated to optimize the trade-off between stiffness, mass, and the retraction ratio.

a) Double Scissor Linkage for Dynamic Angle Adjustment: In this architecture, the wing cells are not attached directly to the primary scissor mechanism but to a secondary row of linkages (see Fig. 11). These secondary links are connected to the extremities of the primary scissors and to each other, with unequal lengths. This configuration allows the cell attachment bars to remain perfectly horizontal when deployed and perfectly vertical when retracted, even though the structural scissors are never parallel.

This system theoretically offers the highest retraction ratio, as the linkages store vertically, meaning only the thickness of one link and the wing profile accumulate. However, this dynamic adjustment introduces significant kinematic challenges. The motion of the outer leading edge (R) (see Fig. 12) is driven by the input angle θ (angle between a blue linkage and horizontal in Fig. 11). Defining the semi-height of the mechanism $s = \frac{L_1}{2}\sin(\theta)$ and the horizontal pivot position $x_r = L_1\cos(\theta)$, the attachment points are $\mathbf{A} = [x_r, s]^T$ and $\mathbf{B} = [x_r, -s]^T$.

The position of the upper leading edge point $\mathbf{R}_1$ is determined by the intersection of the secondary bars (L_2, L_3). The intermediate intersection point $\mathbf{P}_1(x_{P1}, y_{P1})$ is found by solving the geometric constraints:

$$y_{P1} = \frac{L_2^2 - L_3^2}{4s}, \quad x_{P1} = x_r + \sqrt{L_3^2 - (y_{P1} - s)^2} \tag{2}$$

Defining the unit vector $\hat{\mathbf{u}}_1$ along the short bar, the final coordinate $\mathbf{R}_1$ includes a perpendicular offset L_4:

$$\mathbf{R}_1 = \mathbf{A} + d_x\hat{\mathbf{u}}_1 + L_4\mathbf{M}_{-90}\hat{\mathbf{u}}_1 \tag{3}$$

where $\mathbf{M}_{-90}$ is the rotation matrix. Similarly, the lower coordinate $\mathbf{R}_2$ is derived symmetrically using $\mathbf{M}_{+90}$.

Numerical analysis of these equations highlights a critical issue. Figure 13a plots the vertical position (y) of the linkage attachment points (Q_1, Q_2) and the leading edge tips (R_1, R_2) as a function of the deployment angle. With centered linkages, the leading edge undergoes an oscillatory motion, creating kinematic interference where the structure conflicts with the cell geometry.

A viable solution was identified by offsetting the mounting points (see Fig. 13b). This modification eliminates the interference, resulting in a smooth monotonic trajectory for the leading edge tips (R_1, R_2). Figure 14 visualizes the resulting mechanism throughout the deployment range ($10°$ to $75°$) using these optimized parameters. However, this solution prevents the mechanism from utilizing the full internal volume of the cell. Furthermore, this system doubles the number of required bars, increasing total mass and reducing reliability.

Fig. 11: double scissor mechanism

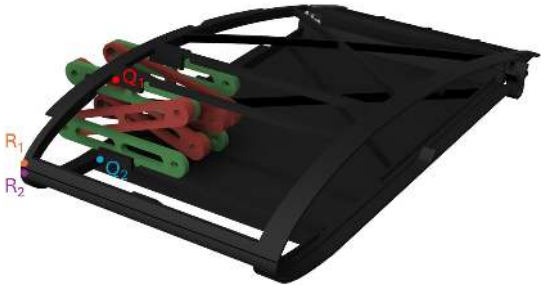

Fig. 12: position of points Q (attachment point between the link and the wing surface) and R (inner tip of the leading edge)

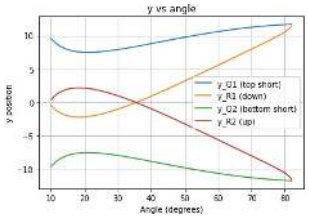

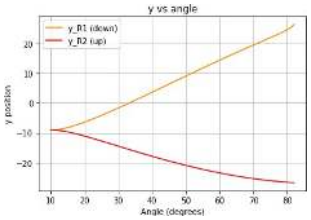

(a) Configuration with interference

(b) Viable solution (offset mounting)

Fig. 13: Vertical displacement of key kinematic points vs. deployment angle. (a) shows the positions of the wing attachment points (Q_1 in blue and Q_2 in green), and the tips (R_1 in orange and R_2 in red), where the conflicts occur. (b) shows the optimized geometry where R_1 and R_2 follow a collision-free path.

b) Optimized Single Scissor Linkage: Consequently, a second architecture was developed and selected for the final prototype to prioritize mass reduction. This system uses a single primary scissor mechanism to both transmit motion and

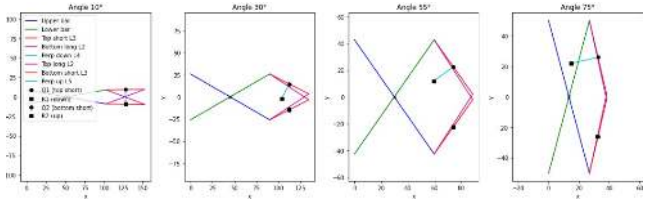

Fig. 14: Kinematic simulation of the optimized double scissor mechanism (corresponding to the viable solution in Fig. 13b) from $10°$ to $75°$.

anchor the cells. The primary constraint of this design is the maximum retraction capacity, defined by the sum of the angles:

$$\theta_{total} = \gamma + \beta \tag{4}$$

where γ is the deployment angle and β is the angle of the closed scissors (see Fig. 15). Since γ cannot be excessively reduced without compromising structural rigidity, minimizing β is critical for maximizing the retraction ratio.

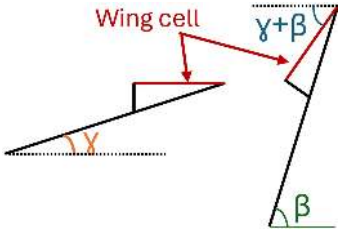

Fig. 15: Geometric constraints on the retraction ratio: the total folding limit is determined by the sum of the deployed angle γ and the retracted angle β.

To address this, the linkages were designed with a specific "M-shaped" profile (see Fig. 16). This geometry allows the linkage to conform to the shape of the preceding cell, enabling the wing to retract into a compact, near-horizontal stack despite the geometric constraints of a single-scissor system.

(a) Optimized "M-shaped" link

(b) Assembly showing nesting capability

Fig. 16: Design of the retained scissor linkage system. The custom profile allows the mechanism to clear the geometry of the previous cell, minimizing the angle β.

3) Geometric Dimensioning of the Linkage System: Optimizing the dimensions of the scissor linkages is a critical step in the wing design. Maximizing the linkage length, L_1, allows for a reduction in the total number of cells, thereby minimizing the overall structural mass. However, the linkage dimensions are strictly constrained by the internal volume of the aerodynamic profile.

To determine the maximum allowable linkage size, we modeled the constraints using the NACA 4-digit airfoil definition. The problem is twofold: first, determining the available vertical clearance (L) and horizontal spacing (X) within the profile; second, relating these geometric bounds to the physical length of the linkage bars (L_1).

a) Airfoil Geometric Constraints: We consider a NACA profile defined by digits $MPXX$, with chord length c, maximum camber M, position of max camber P, and thickness t is XX % of the chord. The half-thickness distribution $y_t(\xi)$ along the chord $\xi \in [0, c]$ is given by [5]:

$$\begin{aligned} y_t(\xi) = 5tc\Bigg(&0.2969\sqrt{\frac{\xi}{c}} - 0.1260\frac{\xi}{c} \\ &- 0.3516\left(\frac{\xi}{c}\right)^2 + 0.2843\left(\frac{\xi}{c}\right)^3 \\ &- 0.1015\left(\frac{\xi}{c}\right)^4\Bigg) \end{aligned} \tag{5}$$

The mean camber line $y_c(\xi)$ and the local camber angle $\theta(\xi) = \arctan(dy_c/dx)$ are defined as:

$$y_c(\xi) = \begin{cases} \frac{m}{p^2}(2p\xi - \frac{\xi^2}{c}) & 0 \le \xi < pc \\ \frac{m}{(1-p)^2}((1-2p) + 2p\frac{\xi}{c} - \frac{\xi^2}{c}) & pc \le \xi \le c \end{cases} \tag{6}$$

The local coordinates for the upper (U) and lower (L) surfaces are:

$$x_{U,L}(\xi) = \xi \mp y_t(\xi)\sin(\theta(\xi)) \tag{7}$$

$$y_{U,L}(\xi) = y_c(\xi) \pm y_t(\xi)\cos(\theta(\xi)) \tag{8}$$

To account for the angle of attack α, these coordinates are transformed into the global frame:

$$\begin{bmatrix} X_{glob} \\ Y_{glob} \end{bmatrix} = \begin{bmatrix} \cos\alpha & -\sin\alpha \\ \sin\alpha & \cos\alpha \end{bmatrix} \begin{bmatrix} x_{loc} \\ y_{loc} \end{bmatrix} \tag{9}$$

The structural integration requires two vertical bars of height L to fit between the intrados and extrados (see Fig. 17a). This is solved by finding the roots of the residual function $\mathbf{F}$ for the upper (ξ_U) and lower (ξ_L) chord positions:

$$\mathbf{F}(\xi_U, \xi_L) = \begin{bmatrix} X_U(\xi_U) - X_L(\xi_L) \\ Y_U(\xi_U) - Y_L(\xi_L) - L \end{bmatrix} = \mathbf{0} \tag{10}$$

Numerical resolution yields two solution sets (front and rear bars), defining the maximum horizontal spacing X:

$$X = |X_U(\xi_{U2}) - X_U(\xi_{U1})| \tag{11}$$

b) Linkage Length Calculation: Once the profile constraints determine the allowable thickness L, the physical length of the scissor linkage L_1 is derived. As illustrated in

Fig. 17b, the relationship depends on the deployment angle γ, the linkage thickness T_1, and the profile shell offset T_2:

$$L = \frac{L_1}{2}\sin(\gamma) + 2(T_1 + T_2) \tag{12}$$

This equation ensures that the mechanism maximizes the use of the internal volume while maintaining the necessary structural clearances.

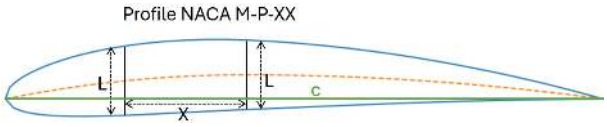

(a) Geometric fitting of vertical bars within the airfoil

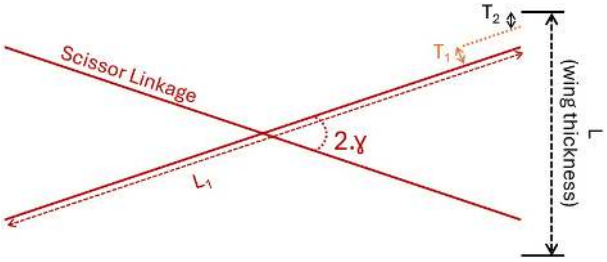

(b) Trigonometric relationship of the scissor linkage

Fig. 17: Dimensional optimization of the retraction mechanism.

4) Structural Optimization and Experimental Parameter Selection: While geometric constraints dictate the maximum possible dimensions, the deployment angle γ plays a decisive role in the structural stiffness and internal load distribution. To quantify this, we consider a simplified static model of the system composed of two parallels sets of single scissor linkages under a vertical external load F (representing lift or weight), as shown in Fig. 18.

The axial force F_{bar} generated within the linkage bars in traction or compression is inversely proportional to the sine of the deployment angle:

$$F_{bar} = \frac{F}{2\sin(\gamma)} \tag{13}$$

Although this model is a simplification of the full multi-segment mechanism, the scaling factor $1/\sin(\gamma)$ governs the internal stress amplification regardless of the number of scissor units. Consequently, low deployment angles result in exponential increases in internal forces, leading to significant structural deflection and an increased risk of buckling.

This relationship drove the iterative design process of the prototype. The initial configuration utilized cells with a 10 cm span and a 24 cm chord, and a deployment angle of $\gamma = 8°$. Experimental testing revealed that this configuration was too flexible and structurally fragile for flight loads. By leveraging the geometric optimization equations defined previously, the cell dimensions were maximized to fit the NACA profile. The final prototype features a 12.5 cm span per cell and a 25 cm chord. This adjustment allowed the deployment angle to increase to $\gamma = 12°$. Analytically, shifting from $8°$ to $12°$ yields a reduction in internal structural loads of approximately 33%. This optimization significantly enhanced the global rigidity of the wing without requiring additional reinforcement mass.

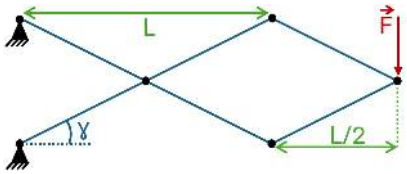

Fig. 18: Simplified static analysis of the scissor linkage. The deployment angle γ critically determines the mechanical advantage and internal stress amplification.

5) Prototype: Structural Design and Manufacturing: The structural architecture of the wing is modular, relying on a hybrid manufacturing approach that combines additive manufacturing for complex aerodynamic shells with subtractive manufacturing for high-stress kinematic components. The linkages were CNC-machined from 2.5 mm thick carbon fiber plates. Despite the geometric limitation to 2D shapes imposed by 3-axis machining, the high specific stiffness of the carbon fiber rendered additional reinforcement unnecessary. An exploded view of the assembly is presented in Fig. 19.

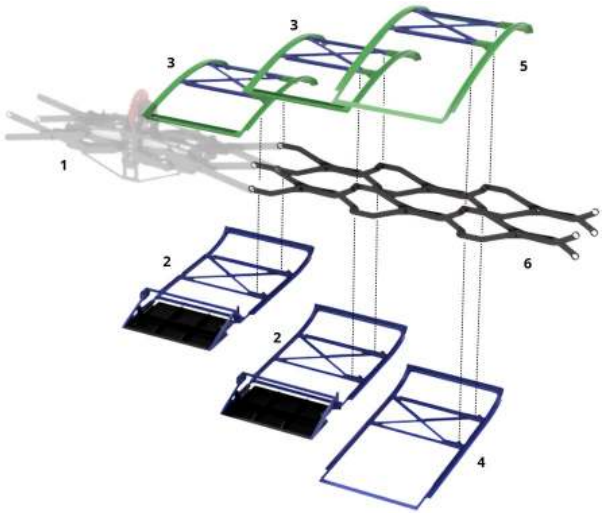

Fig. 19: Exploded view of the retractable wing assembly: (1) deployment actuation mechanism, (2) lower surface cell with integrated flap, (3) upper surface cell with integrated flap, (4) standard lower surface cell, (5) standard upper surface cell and (6) the two sets of parallel carbon fiber scissor linkages.

a) Cell Structure and Geometric Optimization: The wing cells (Fig. 19, element (2, 3, 4, 5) were manufactured using Fused Deposition Modeling (FDM). The selected material is Polyethylene Terephthalate Carbon Fiber (PET-CF), chosen for its specific modulus, which is approximately three times higher than standard PETG. To overcome the anisotropy inherent in FDM, the cells were sliced into multiple discrete components, specifically, the airfoil profiles and the internal connecting bars, and subsequently bonded using cyanoacrylate adhesive. This modular assembly allowed for the optimization of print orientation, ensuring that layer lines were aligned to minimize

shear stress and maximize tensile strength along critical load paths.

The internal geometry of these components was rigorously optimized to maximize the second moment of area (I) while minimizing mass. As shown in Fig. 20, T-shaped and L-shaped cross-sections were employed for the external structural spars and the internal X-bracing. This design minimizes flexion along both the chord and the span.

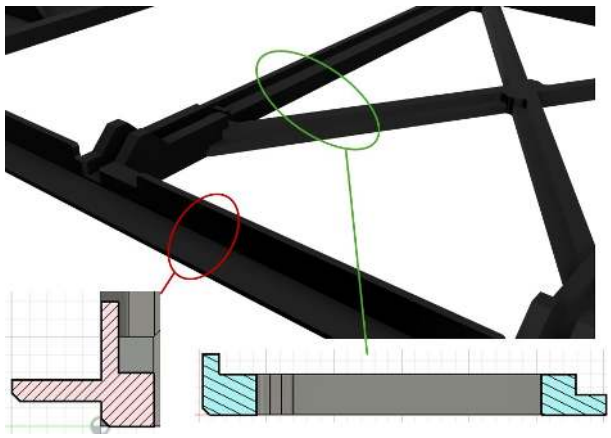

Fig. 20: Cross-sectional optimization of 3D printed components. ”T” and ”L” geometries were selected to maximize the second moment of area to mass ratio.

A critical feature of the design is the mechanical nesting of adjacent cells. As illustrated in Fig. 21, the cells are designed to interlock with one another when deployed. This imbrication serves a dual purpose: first, it significantly enhances global structural rigidity by preventing relative rotation between segments, thereby relieving the scissor linkages (part 6) of torsional loads. Second, it ensures aerodynamic continuity by eliminating gaps between the wing segments.

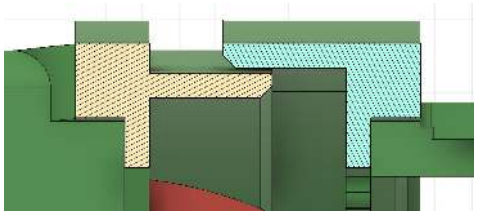

Fig. 21: Cross-section detail of the nesting interface. The stepped geometry ensures that cells interlock, increasing torsional rigidity and preventing aerodynamic gaps.

The final prototype utilizes a NACA 4418 profile with a 250 mm chord and a total deployed span of 1.5 m, divided into 12 cells of 125 mm each. These dimensions were selected to satisfy the aerodynamic lift requirements while complying with the manufacturing constraints imposed by the build volume of the available 3D printers.

b) Linkage Integration and Finite Element Analysis: Each semi-cell is anchored to two parallel rows of scissor linkages (Fig. 19, element (6)). This dual-row configuration distributes the aerodynamic load approximately evenly around the cell’s center of mass and center of lift, significantly reducing torsional deflection and bending moments around the vertical z-axis.

To validate the structural dimensioning, a Finite Element Method (FEM) analysis was conducted on a simplified assembly of six linkage rows (representing one of the two parallel lines). A total load of 1.2 kg was applied, distributed as 80% on the suction side (extrados) and 20% on the pressure side (intrados), and uniformly shared across the cells. This corresponds to an equivalent acceleration of 2 g.

The results (see Fig. 22) indicate that stress concentrations are highest at the root linkages and decay rapidly; the stress in the second row is approximately 50% lower than in the first (Fig. 22b). The maximum recorded von Mises stress was 68 MPa. Given the material properties of the carbon fiber composite, this yields a safety factor significantly greater than 20, confirming the structural integrity of the design under flight loads.

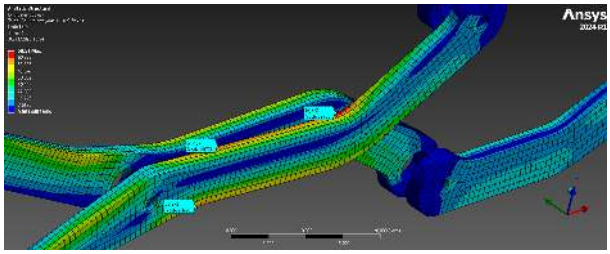

(a) Stress distribution on root linkage

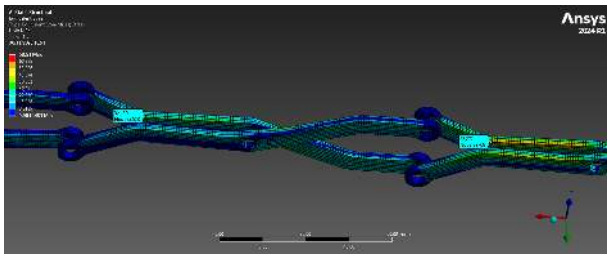

(b) Stress decay between row 1 and 2

Fig. 22: FEM analysis of the carbon linkage assembly under a simulated load of 1.2 kg. The stress concentration (max 68 MPa) is localized at the root and decreases rapidly along the span.

c) Linkage Joint Design: To minimize operational friction during the deployment and retraction of the scissor mechanism, a specific joint architecture was implemented, as illustrated in the schematic cross-section in Fig. 23. A standard deep-groove ball bearing ($2 \times 5 \times 2.5$ mm) is pressed into the first linkage arm. The screw assembly is tightened such that the screw head presses exclusively against the inner race of this bearing, preventing direct rubbing against the carbon fiber linkage body. A low-friction spacer bearing is inserted between the two linkage arms to eliminate surface contact during rotation. Finally, the screw passes through a clearance hole in the second linkage arm and is secured with a nut, making the screw rigidly solidary with the second arm while remaining decoupled from direct contact with the first.

While this configuration ensures a smooth and highly efficient kinematic motion, it introduces a structural compro-

mise. Due to manufacturing tolerances, standard ball bearings possess a nominal internal clearance slightly larger than the mating axial shafts. This slight individual play accumulates across the series of linkages, introducing undesired slop and resulting in global structural bending under aerodynamic load.

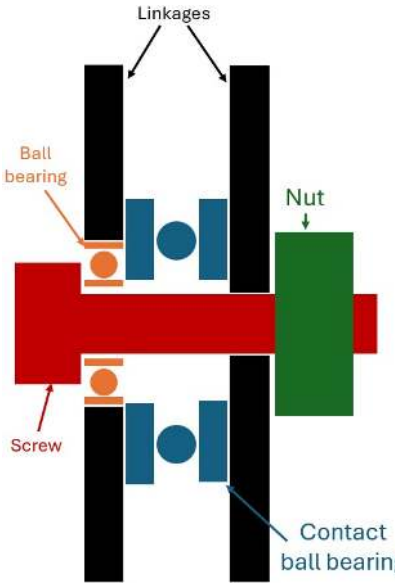

Fig. 23: Schematic cross-section of the low-friction linkage joint. Stackup includes the screw assembly acting on the inner race of the standard bearing inserted in the primary linkage, separated from the secondary linkage by a low-friction spacer.

d) Aerodynamic Skinning: Finally, the rigid framework acts as a skeleton for the aerodynamic skin. We selected a heat-shrink film covering, a standard technique in aeromodeling, to create a smooth, continuous surface. The application process required wrapping each semi-cell individually; precise tension management was critical to prevent the film's shrinkage force from warping the printed structure. Alternative materials were evaluated, including $0.15\,\text{mm}$ PETG sheets, but were rejected due to excessive weight penalties. Non-shrink films were also discarded as they failed to produce a sufficiently smooth surface profile.

6) Actuation and Deployment Mechanism: The retraction capability is powered by a custom electro-mechanical assembly designed to decouple the actuation forces from the aerodynamic structural loads. An exploded view of the mechanism is presented in Fig. 24.

a) Kinematics and Load Path: The actuation sequence is driven by a DC motor (8) which rotates the transmission gear (7), driving a central double reverse lead screw (6). The reverse threading ensures that the two drive nuts (2) move symmetrically relative to the center, either converging or diverging. These nuts drive the deployment linkages (5). Each linkage is anchored at a fixed pivot point on the fuselage and connected to the drive nut via a sliding pivot slot. Crucially, the structural sliders (4) act as the interface between the wing assembly and the fuselage. By design, the aerodynamic loads (lift and drag) and structural weight are transmitted directly through the sliders to the central fuselage beam. This

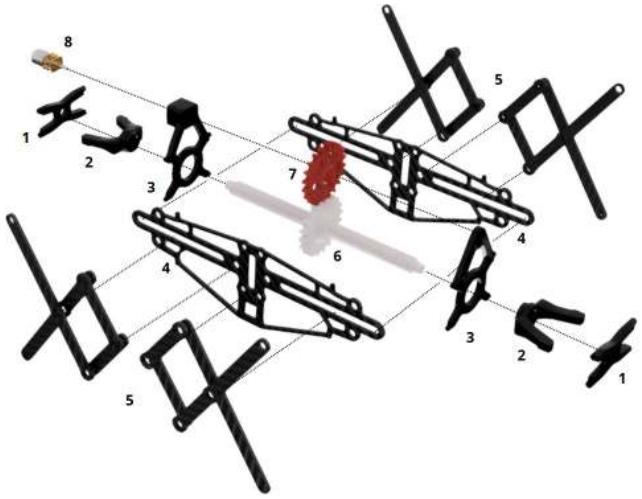

Fig. 24: Exploded view of the deployment mechanism: (1) external lead screw supports, (2) drive nuts, (3) internal motor mount and bearing support, (4) structural sliders, (5) deployment linkages, (6) double reverse lead screw, (7) transmission gear, and (8) DC motor.

mechanical decoupling ensures that the lead screw (6) and motor (8) are isolated from flight loads and only experience the torque required to overcome friction during deployment.

b) Material Selection: Materials were selected based on specific mechanical and tribological requirements. The structural components, specifically the sliders (4) and deployment linkages (5) are machined from carbon fiber to withstand high bending moments and shear forces. To ensure sufficient stiffness for bearing alignment, the supports (1, 3) are manufactured using PET-CF. Finally, the drive mechanics (2, 6) utilize a resin-printed lead screw for geometric precision paired with drive nuts 3D-printed from PTFE-filled PETG filament; this tribological combination significantly reduces the coefficient of friction, thereby minimizing the system's torque requirement.

c) Structural Optimization: The structural slider (4) is identified as one of the most critical components in the drone, acting as the primary load transfer path. To minimize mass while ensuring structural integrity, a topology optimization workflow was employed. An initial geometry was generated using Generative Design algorithms (see Fig. 25a), serving as a baseline for the structural layout.

Subsequent Finite Element Method (FEM) iterations were conducted to refine the geometry. By optimizing the support placement at the slider extremities and removing non-contributing material, the stress distribution was significantly improved. Comparing the first iteration (Fig. 25b) to the final design (Fig. 25c), the maximum Von Mises stress was reduced by 25% under identical load conditions, resulting in a lighter and more robust component.

7) Morphing Control Surfaces (Flaps): To maintain the compactness of the retractable architecture, the design necessitates that control surfaces be integrated directly into the wing cells rather than relying on fixed empennage surfaces. This requirement introduces significant challenges regarding

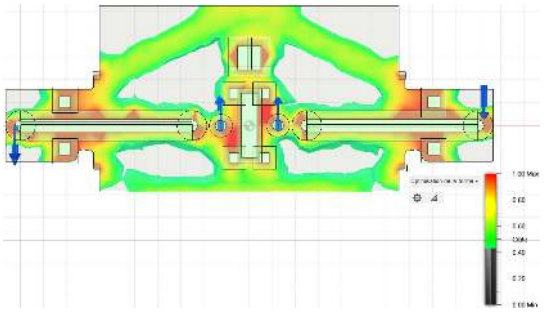

(a) Generative Design input

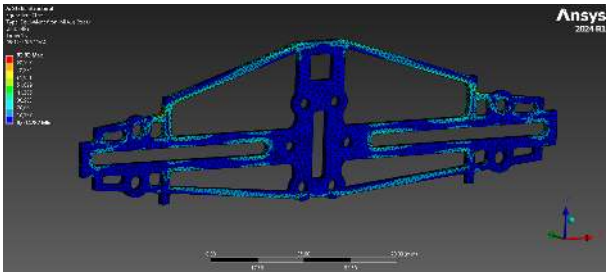

(b) Iteration 1: High stress concentrations

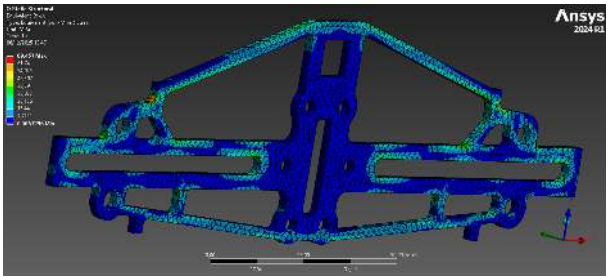

(c) Iteration 3: Optimized distribution (-25% stress)

Fig. 25: Optimization workflow of the structural slider. The final iteration (c) demonstrates a significant reduction in peak stress compared to the initial design (b).

actuation and kinematic continuity.

a) Inter-Cell Kinematic Transmission: A single cell width does not provide sufficient control surface area. Consequently, the flaps of the inner cells must operate in unison. Placing actuators inside the wing was ruled out due to the complexity of cable management during retraction and the added weight on the cantilevered structure. Instead, the actuation is deported to the fuselage, requiring a mechanism to transmit torque from the fuselage to the first flap, and subsequently from one flap to the next.

We developed a sliding interlocking system (see Fig. 26). The driving flap engages the driven flap via an oblong pin that slides into a mating slot. The oblong geometry is critical: unlike a cylindrical pin which would only transmit transverse loads, the oblong shape transmits both translation and rotation while accommodating slight misalignment caused by structural deformation. Since the assembly occurs vertically, the pin is unconstrained in the vertical z-axis, allowing for the wing's deployment without jamming.

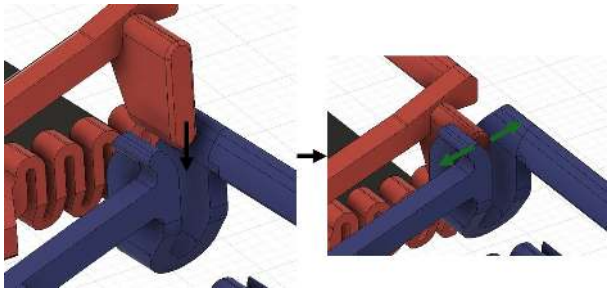

Fig. 26: Inter-cell transmission mechanism. The oblong pin (green arrows) transmits torque while accommodating the variable distance between cells during deployment.

b) Multi-Material Compliant Hinge Design: The hinge is implemented as a compliant flexure integrated directly into the airfoil structure. Material selection was a primary constraint: the wing structure (PET-CF) is too stiff for a flexure, while standard flexible filaments (e.g., Thermoplastic polyurethane(TPU)) lack the restorative force required to return the flap to a neutral position. We selected PETG for the hinge interface. It offers a balance of compliance for actuation and elasticity for passive return. However, co-printing PETG (melting point $\approx 235°$C) with PET-CF (melting point $\approx 290°$C) presents adhesion challenges.

Several interface geometries were tested to ensure mechanical interlocking (see Fig. 27a). Complex interlocks (cross or ball shapes) introduced print inaccuracies. The final optimized design utilizes a deep, straight internal spar (Fig. 27b). This geometry maximizes the surface area for thermal fusion—aided by the high temperature of the PET-CF—ensuring a bond that withstands the shear stresses of actuation.

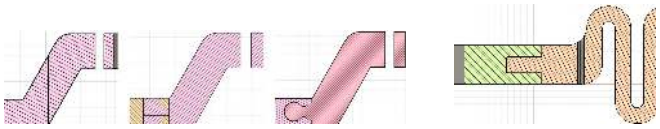

(a) Interface topology evaluation (b) Final retained geometry

Fig. 27: Multi-material interface design. Various locking geometries were tested (a) to bond the PETG hinge to the PET-CF structure. The final design (b) uses a deep straight insertion to ensure thermal fusion and mechanical stability.

c) Geometric Optimization of the Flexure: Two flexure geometries were analytically compared: a circular arc and a sinusoidal profile.

The circular arc (Fig. 28a) assumes a constant arc length s, implying $\Omega R = \Omega_1 R_1$. Assuming the attachment points are rigid, the center of curvature C (Fig. 28c) moves according to:

$$C = \left[R\cos\left(\frac{\Omega}{2} - \frac{\pi}{2}\right), \quad R\sin\left(\frac{\Omega}{2} - \frac{\pi}{2}\right) \right]^T \tag{14}$$

While this geometry distributes stress uniformly, it couples rotation with significant translation, creating a large aerodynamic gap between the wing and the flap upon deflection.

The sinusoidal profile (Fig. 28b) accommodates more material length in a compact space, reducing local strain for a given deflection angle. Its motion can be approximated as a beam in pure bending. For a beam of length L deflected by angle θ, the tip coordinates are:

$$\begin{cases} x_M(\theta) = \frac{L}{\theta}\sin(\theta) \\ y_M(\theta) = \frac{L}{\theta}(1-\cos(\theta)) \end{cases} \tag{15}$$

For small θ, this motion approximates pure rotation more closely than the circular arc. Consequently, the sinusoidal geometry was selected to minimize the aerodynamic gap and maintain flow attachment.

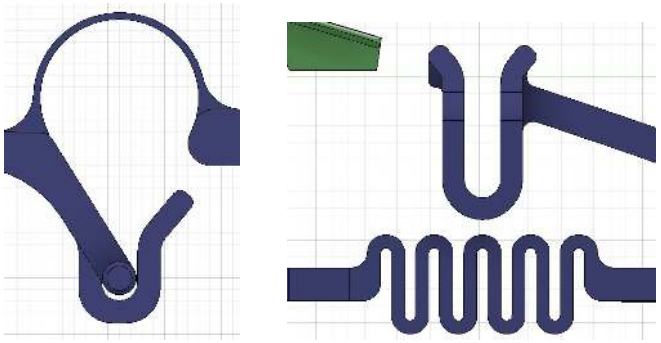

(a) Circular arc geometry (b) Sinusoidal geometry (Retained)

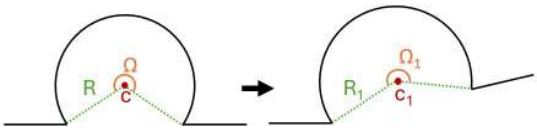

(c) circular hinge motion

Fig. 28: Comparison of flexure geometries. The sinusoidal profile (b) was selected as it approximates pure rotation, minimizing the aerodynamic gap compared to the circular arc (a).

d) Flap Integration: To ensure structural rigidity under aerodynamic load, the flap body is printed monolithically with the compliant hinge. A $0.15\,\text{mm}$ layer of PETG is printed directly onto the flap surface to act as an aerodynamic skin, providing a smooth finish and additional stiffness against flutter.

8) Design Synthesis and Achieved Retraction Ratio: The development of this prototype was the result of an extensive iterative process, involving more than ten distinct design generations to converge on a solution that effectively balances structural stiffness, minimal weight, and kinematic reliability. This rigorous testing phase was particularly crucial for ensuring the smooth deployment of the morphing control surfaces under load.

Ultimately, the proposed system achieves a global retraction ratio of more than $5:1$, with a total mass of $1.05\,\text{kg}$ (including the wings and deployment mechanism). This performance is particularly notable given that the chosen architecture (the optimized single-scissor linkage) was selected over the double-scissor alternative.

E. Software

The system is based on a Pixhawk flight controller running the PX4 autopilot firmware and configured using QGroundControl. PX4 provides a modular and flexible framework supporting multirotor, fixed-wing, and VTOL configurations. In this project, standard PX4 airframes available in QGroundControl were used as a baseline for the quadcopter, fixed-wing airplane, and VTOL modes. Each airframe required specific adaptations to account for the custom mechanical layout of the prototype. In particular, the placement and orientation of the motors were configured to match the physical position of the hover propellers and the forward propulsion system. The Pixhawk installation parameters were also adjusted in software to correctly account for the offset and orientation of the onboard IMU relative to the drone frame. Additionally, the control ranges of the servo motors actuating the aerodynamic control surfaces were configured, and their effectiveness was calibrated for airplane flight mode.

In a first stage, flight tests were conducted to validate operation in quadcopter mode only. These tests were successful and confirmed stable hovering, adequate control authority, and correct motor configuration. Following this validation phase, the focus was shifted to fixed-wing flight in order to characterize the aerodynamic behavior and control surface effectiveness independently. Stabilization and attitude control rely on PX4's cascaded PID control architecture. During the initial fixed-wing flight tests, conducted using rigid wings with the same dimensions as the folding wings, unstable behavior and unsuccessful flights were observed. These instabilities were mainly attributed to mechanical vibrations affecting sensor measurements. Consequently, the PID gains, particularly the pitch proportional gain (K_p), were manually tuned through successive test flights to improve stability and responsiveness. This process resulted in a 50% reduction of the K_p gain compared to the standard value proposed by the PX4 airframe configuration.

The aerodynamic efficiency and effectiveness of the control surfaces were further investigated using the WindShape system, a modular wind-generation platform capable of producing controlled and spatially distributed airflow. This setup enabled rapid qualitative assessment of control surface authority and symmetry under repeatable flow conditions, without the risks associated with free-flight testing. The results obtained with WindShape were used to refine control surface parameters in QGroundControl and contributed to improved predictability in airplane mode.

All mode switching logic, state estimation, and low-level attitude control are handled internally by the PX4 autopilot. No custom navigation algorithm or external state machine was implemented beyond airframe configuration and parameter tuning. Once the individual airframes were validated, the VTOL mode was configured and tested on the ground using a dedicated switch on the RC transmitter to command mode transitions. The PX4 VTOL configuration in QGroundControl provides access to several parameters governing transition behavior, including transition duration, minimum airspeed required to complete the transition, throttle and thrust distri-

bution among the different motors during and after transition, as well as blending and mixing factors used to smooth the transition between hover and forward flight. However, no flight tests involving VTOL transitions were performed. One specific challenge identified during software configuration concerned the pitch angle commanded during forward acceleration in hover mode. A downward tilt is required to generate forward thrust; however, excessive tilt reduces the effective lift generated by the wings. To address this issue, dedicated PX4 parameters were investigated and adjusted to limit the maximum pitch angle during transition, ensuring a compromise between forward acceleration and wing lift generation.

Although a GPS module was not implemented on the current prototype, the plug-and-play capabilities of the Pixhawk platform would allow straightforward integration of a GNSS receiver in future iterations. This would enable autonomous flight features such as waypoint-based missions and auto-landing, as well as improved estimation of ground speed and traveled distance. This limitation was acceptable for the present proof-of-concept, which focuses on manual and semi-assisted flight modes.

IV. Aerodynamic Study

A. Aerodynamic Efficiency : 2D Simulations

1) 2D Mesh Validation: Two-dimensional CFD simulations were first performed to validate the numerical setup and obtain reliable aerodynamic coefficients for preliminary wing dimensioning. The NACA 4418 airfoil was selected due to its 18% thickness-to-chord ratio, which allows the integration of the wing deployment mechanism.

The simulations were carried out using ANSYS Fluent and validated against experimental data reported in *NACA Report No. 824 – Summary of Airfoil Data* [6], obtained in the Langley low-turbulence wind tunnel. The flow conditions correspond to standard atmosphere ($T = 288.15\,\mathrm{K}$, $\rho = 1.225\,\mathrm{kg\,m^{-3}}$, $\mu = 1.789 \times 10^{-5}\,\mathrm{Pa\,s}$) at a Reynolds number of $Re = 3 \times 10^6$, yielding a free-stream velocity of $U_\infty = 71.885\,\mathrm{m\,s^{-1}}$ for a chord length of $c = 609.6\,\mathrm{mm}$ and a wingspan of $b = 910\ \mathrm{mm}$.

The airfoil surface was modeled as a wall with a no-slip boundary condition. A surface roughness height of $7.25 \times 10^{-5}\,\mathrm{m}$ was prescribed in order to account for the finite roughness of a real airfoil and avoid the assumption of a perfectly smooth wall. While this roughness improves agreement with the experimental data by influencing boundary-layer development and transition, it also introduces a degree of overfitting. Consequently, although the model is well calibrated for the present airfoil, its predictive capability may be reduced when applied to different airfoil geometries. A near-wall modeling approach using a C-type quadrilateral structured mesh, shown in Fig. 29, combined with the Transition SST (γ–Re_θ) turbulence model was employed. A strong mesh biasing strategy (meaning very short cells at the airfoil surface and larger cells far from the airfoil, visible in Fig. 29b) is applied to achieve the fine near-wall resolution required to accurately capture boundary-layer development and laminar-to-turbulent transition under low free-stream turbulence conditions, as encountered in the Langley low-turbulence wind tunnel.

Further details about the 2D simulations are provided in the Appendix.

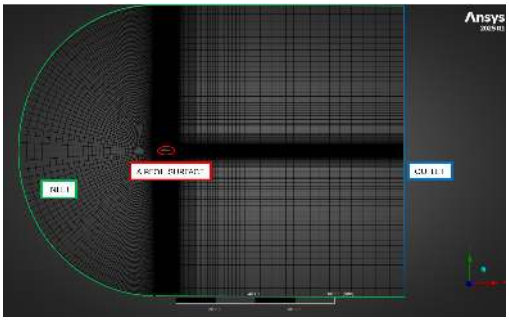

(a) The overall mesh domain

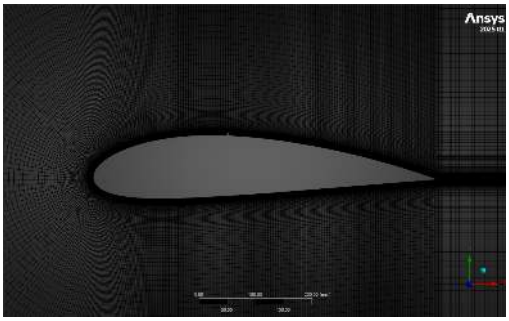

(b) Close up to the airfoil region

Fig. 29: C-type structured quadrilateral mesh

2) 2D Validation Results: The numerical lift and drag coefficients were compared with experimental data, Table V and Table VI, over an angle-of-attack range between $2°$ and $8°$. The results show good agreement, with mean absolute relative errors of 4.07% for the lift coefficient and 6.24% for the drag coefficient, indicating that the numerical setup is sufficiently accurate within the considered operating range.

TABLE V: Relative error of 2D lift coefficient

AOA	Experimental	Simulation	Relative error (%)
2	0.615459	0.639200	+3.86
4	0.806835	0.834500	+3.43
6	1.002766	1.050000	+4.71
8	1.175915	1.226500	+4.30

Mean absolute relative error on C_l: 4.07 %

TABLE VI: Relative error of 2D drag coefficient

C_l	Experimental	Simulation	Relative error (%)
0.615459	0.007756	0.007595	-2.07
0.806835	0.008151	0.008088	-0.77
1.002766	0.009156	0.009707	+6.02
1.175915	0.010521	0.012215	+16.11

Mean absolute relative error on C_d: 6.24 %

3) 2D VTOL Wing Dimensioning: The validated 2D mesh was then used for preliminary wing dimensioning of the VTOL drone. The airfoil chord was reduced to $c = 250\,\mathrm{mm}$ to satisfy structural constraints imposed by the wing deployment mechanism. With a thickness-to-chord ratio of 18%, this

results in a maximum airfoil thickness of $45\,\mathrm{mm}$, which represents the minimum height required to accommodate the deployment system inside the wing. In addition, since the airfoil chord is smaller than the one used in the validation mesh ($c = 609.6\,\mathrm{mm}$), the computational domain was rescaled in order to preserve the relative proportions of the mesh.

At an arbitrarily chosen cruise velocity of $12\,\mathrm{m\,s^{-1}}$ and an angle of attack of $4°$, the simulations yield an averaged lift per unit span of $L_b = 11.8\,\mathrm{N\,m^{-1}}$ (Averaged value computed over the last 500 iterations of a total of 2000 iterations, as the residual convergence criterion of 10^{-6} was not reached.). Balancing lift and weight for an estimated drone mass (at the beginning of the semester) of $1.5\,\mathrm{kg}$ results in a required wingspan of approximately $b = 1.3\,\mathrm{m}$, accounting for an uncertainty lift of approximately 4%, as reported in Table V. Since each retractable wing cell has a width of $125\,\mathrm{mm}$, an initial wingspan of $b = 1{,}250\,\mathrm{mm}$ was selected at the beginning of the semester.

As the project progressed and the estimated VTOL aircraft mass increased beyond the initial expectation (around $2\,\mathrm{kg}$), the wingspan was subsequently increased to $b = 1{,}500\,\mathrm{mm}$. Based on the averaged lift per unit span obtained from the 2D simulations ($L_b = 11.8\,\mathrm{N\,m^{-1}}$), a wingspan of approximately $1{,}730\,\mathrm{mm}$ would have been required to meet the lift requirements at a cruise velocity of $12\,\mathrm{m\,s^{-1}}$ for $2\,\mathrm{kg}$. However, due to structural constraints related to wing bending, the wingspan was limited to $1{,}500\,\mathrm{mm}$. This compromise implies that a higher cruise velocity than initially assumed may be required to generate sufficient lift.

B. Aerodynamic Efficiency : 3D Simulations

1) 3D Mesh Validation: Three-dimensional simulations were performed to validate the 3D mesh and assess its ability to capture finite-wing aerodynamic effects, with a particular focus on lift-induced drag associated with tip-vortex formation. The validation is based on the comparison of two independent formulations of the induced drag coefficient. The first formulation is obtained from the decomposition of the total drag coefficient as

$$C_{D_i}(C_D) = C_D - C_d, \tag{16}$$

where C_D is the total drag coefficient computed from the 3D simulation and C_d is the two-dimensional profile drag coefficient extracted from NACA experimental data. The second formulation follows the classical Prandtl lifting-line theory,

$$C_{D_i}(C_L) = \frac{C_L^2}{\pi e AR}, \tag{17}$$

where C_L is the lift coefficient obtained from the 3D simulation, e is the Oswald efficiency factor, and AR is the wing aspect ratio.

For the present rectangular wing configuration, the Oswald efficiency factor was set to $e = 0.75$ (for a rectangular wing shape). The aspect ratio is defined as $AR = \frac{b}{c}$ which is equal to $AR = 1.49$ for a wingspan of $b = 0.910\,\mathrm{m}$ and a chord length of $c = 0.6096\,\mathrm{m}$ and correspond, for a recall, to the dimensions of the wing used in the experiments conducted by the NACA and reported in *NACA Report No. 824 – Summary of Airfoil Data* [6]. Consistency between the induced drag values obtained from these two formulations provides a strong indication that the 3D mesh and the numerical setup correctly capture the physical effects of the total drag associated with finite-wing theory.

A hemispherical computational domain was adopted, allowing only half of the wing span (i.e., $455\,\mathrm{mm}$) to be simulated through the use of a symmetry boundary condition, thereby significantly reducing the computational cost. The resulting domain, shown in Fig. 30a, contains approximately 15 million cells. For the 3D simulations, the wing surface boundary condition was modeled with a surface roughness of 0.0007. This value was selected because it provided nearly identical induced drag values from Eqs. (16) and (17) at the chosen angle of attack of $4°$. All other parameters, such as the turbulence model and the numerical methods used in the 2D simulations, are applied in the same manner to the 3D simulations.

An unstructured mesh was generated and converted into a polyhedral mesh in ANSYS Fluent in order to improve numerical stability and convergence while maintaining an accurate representation of complex three-dimensional flow features. Local refinements, including edge and surface sizing as well as multiple bodies of influence, were applied to accurately resolve the near-field flow (directly around the wing) and wake region. Inflation layers were introduced on the airfoil surface to capture boundary-layer effects as accurately as possible. However, due to computational constraints, the resulting near-wall resolution corresponds to $y^+ \approx 3$, which limits the accuracy of absolute drag predictions, as the governing equations cannot be fully resolved within the boundary layer down to the airfoil surface, unlike in the 2D simulations.

Further details about the 3D simulations are provided in the Appendix.

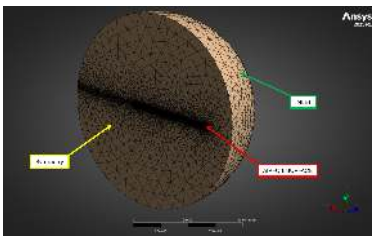

(a) The overall mesh domain

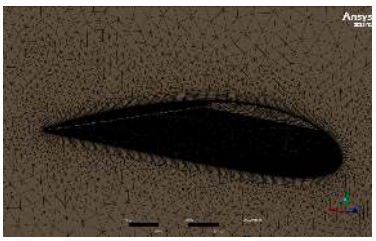

(b) Close up to the wing region

Fig. 30: Hemispherical unstructured polyhedral mesh

2) 3D Validation Results: The comparison between the two induced drag formulations shows significant discrepancies, except at an angle of attack of $4°$, where a relative error of approximately 3% is obtained, as reported in Table VII. The relative errors are computed as

$$\text{Error} = \frac{|C_{D_i}(C_D) - C_{D_i}(C_L)|}{C_{D_i}(C_L)} \times 100, \tag{18}$$

where the induced drag coefficient derived from the lift coefficient, $C_{D_i}(C_L)$, is used as the reference since it directly follows from lifting-line theory and represents the theoretical expectation. The observed deviations are attributed to the combined effects of limited near-wall resolution ($y^+ > 3$) at some locations on the wing surface and the use of surface roughness to match experimental data, which may introduce overfitting.

TABLE VII: Comparison of induced drag coefficients obtained with equations (16) and (17)

α [deg]	C_L	C_D	$C_{D_i}(C_D)$	$C_{D_i}(C_L)$	Error (%)
2	0.19682	0.03914	0.07000	0.04400	59.09
4	0.27148	0.047123	0.08615	0.08382	2.78
6	0.34815	0.05800	0.10685	0.13784	22.47
8	0.42801	0.071771	0.12850	0.20833	38.33

Overall, while the 3D simulations reliably capture lift trends and induced aerodynamic effects, the total drag results are mainly suitable for relative comparisons rather than absolute predictions.

3) 3D VTOL Wing Dimensioning: As in the 2D case, since the VTOL wing chord is $250\,\text{mm}$, the entire *3D Mesh Validation* setup was rescaled based on the chord length in order to preserve the same geometric proportions and ensure similarity in flow resolution. The 3D results confirm that, when accounting for lift-induced drag (which reduce the aerodynamic lift compared to the ideal 2D case) effects associated with a finite wing a sufficient lift can still be achieved. The computed lift is $14.21\,\text{N}$ for a wingspan of $b = 1\,250\ mm$, corresponding to an equivalent mass of $1.45\,\text{kg}$. As expected, this value is lower than the lift predicted by the 2D simulations due to three-dimensional effects, yet it remains close to the target mass and validates the feasibility of the wing design under more realistic conditions.

4) Simplified Model of the Retractable Wing Analysis: To better approximate and understand the flow around the retractable wing, a three-dimensional wing geometry was designed and analyzed using the same computational mesh and numerical methods as those employed for the *3D VTOL Wing Dimensioning* simulations. This approach enables a more faithful representation of a realistic configuration of the retractable wing concept. As shown in Fig. 31, the flaps as well as the most significant openings present in the wing structure were explicitly modeled. In this simplified model, only the interior of the flap is hollow, which remains far from the actual configuration, as in reality the entire wing structure is hollow.

(a) Top view of the retractable wing.

(b) Bottom view of the retractable wing.

Fig. 31: 3D simplified model of the retractable wing

The results show that the presence of such openings in the wing indeed reduces its aerodynamic efficiency. The lift obtained with this simplified realistic model is $12.46\,\text{N}$, corresponding to an equivalent mass of $1.27\,\text{kg}$. Compared to the ideal wing configuration at the cruise velocity, this represents a reduction of approximately $200\,\text{g}$ in lift capacity, which is a non-negligible loss.

The streamlines, shown in Fig. 32, reveal that the openings in the wing allow the air entering the flap (maybe from the pressure-side) cavity to exit through these holes on the suction-side of the wing. Since the static pressure inside the flap is higher than on the upper surface of the wing, where the higher flow velocity induces a lower pressure, the air is expelled normal to the surface. This outflow introduces a vertical component in the local flow, leading to a local pressure increase and, in some regions, even to boundary-layer separation (inside the red circle). This mechanism provides a plausible explanation for the observed loss of lift. It should be noted that this configuration represents a simplified version of the retractable wing, and that in a more realistic design the number of openings would be even larger, potentially amplifying this effect.

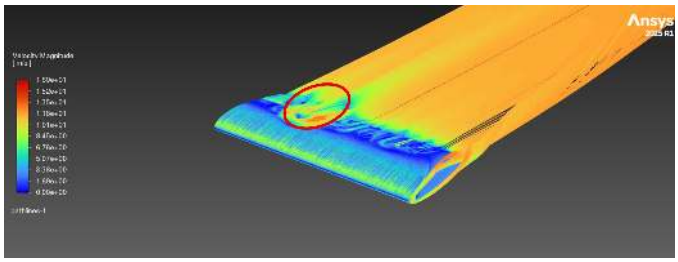

Fig. 32: Pathlines around the simplified model of the retractable wing.

5) Aerodynamic Efficiency of the Retractable Wing: An analysis of the lift-to-drag curve ratio C_L/C_D was performed over several angles of attack (0, 2, 4, 6 and 8 degrees) in order to validate the choice of the operating angle of attack, which is 4 degree, for the retractable wing, that was initially selected based on commonly adopted AOA in RC aircraft wing design.

An analysis of the lift-to-drag ratio C_L/C_D was performed over several angles of attack (0, 2, 4, 6, and 8 degrees) in

order to validate the choice of the operating angle of attack for the retractable wing, which was initially selected based on an ideal wing model. As shown in Fig. 33, the maximum lift-to-drag ratio is reached at an angle of attack of approximately $5°$.

However, an operating angle of attack of $4°$ was retained. As discussed by Anderson in *Fundamentals of Aerodynamics* [7], operating slightly below the angle corresponding to the maximum C_L/C_D provides a more robust and practical flight condition, as it reduces sensitivity to small variations in flow conditions and offers increased margin with respect to boundary-layer separation and stall onset. This choice therefore represents a conservative compromise between aerodynamic efficiency and operational robustness, which is commonly adopted in aerodynamic design.

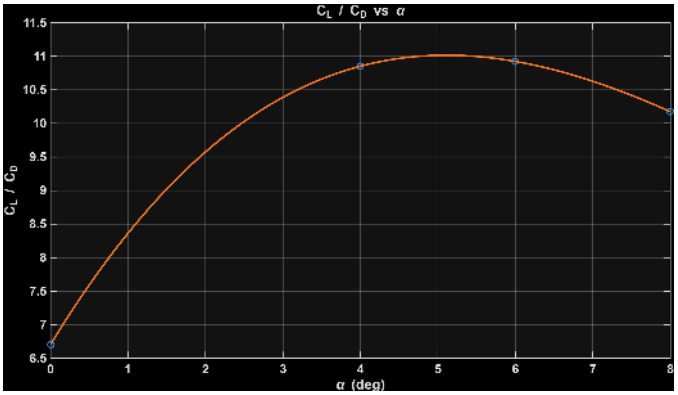

Fig. 33: Curve of the aerodynamic efficiency of the retractable wing

C. Aerodynamic Improvements

1) Retractable Wing Openings Coverage: One potential area for improving the aerodynamic efficiency of the retractable wing is to cover the openings present in the retractable wing, as shown if Fig. 34. One of the main proposed solutions consists in covering these holes with a single-layer 3D-printed PETG film. The objective is to bond this thin PETG layer to both the intrados and extrados surfaces in order to seal the gaps between the flap and the fixed parts of the wing. Owing to its flexibility, the PETG layer does not restrict the flap angle of motion.

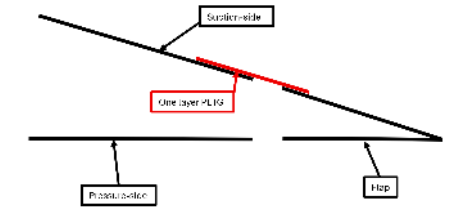

(a) Flap at rest.

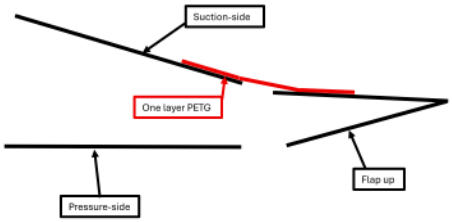

(b) Flap up.

Fig. 34: Flap opening covered with a single-layer PETG sheet.

2) Winglets: Another important area for aerodynamic improvement is the reduction of lift-induced drag through the introduction of winglets (see Fig. 35), whose primary purpose is to mitigate wingtip vortices. According to finite-wing theory, the pressure difference between the lower and upper surfaces drives a spanwise flow near the wingtip, resulting in the formation of strong tip vortices. These vortices induce a downward velocity component in the wake (downwash), which effectively tilts the lift vector rearward and generates induced drag, thereby reducing the aerodynamic efficiency of the wing.

Winglets act by weakening the spanwise flow at the wingtip and redistributing the lift more uniformly along the span. By reducing the strength of the tip vortices, winglets decrease the induced downwash and thus the induced drag. This results in an increase of the effective lift-to-drag ratio without increasing the wingspan, making winglets a well-established solution for improving the aerodynamic efficiency of finite wings.

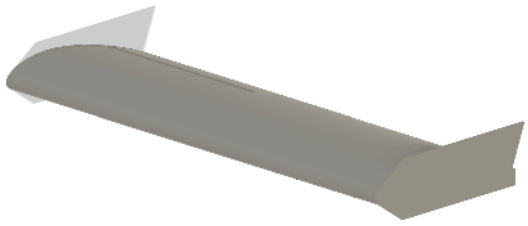

Fig. 35: Overview of the winglet design for the VTOL configuration.

A simulation was performed using the same mesh and numerical method as that employed for the *Simplified Model of the Retractable Wing Analysis* in order to evaluate the potential aerodynamic lift improvement. The results demonstrate that the winglet design provides a noticeable aerody-

namic improvement. While the presence of openings in the retractable wing resulted in a lift loss of approximately $200\,\mathrm{g}$, the introduction of winglets increased the lift to $13.17\,\mathrm{N}$, corresponding to an equivalent mass of $1.34\,\mathrm{kg}$. This represents a recovery of nearly $100\,\mathrm{g}$ of lift, partially compensating for the aerodynamic penalties induced by the wing openings.

As shown in Fig. 36, the tip vortices are significantly weaker than those observed in Fig. 32, leading to an improvement in lift and a more favorable lift distribution along the wing span.

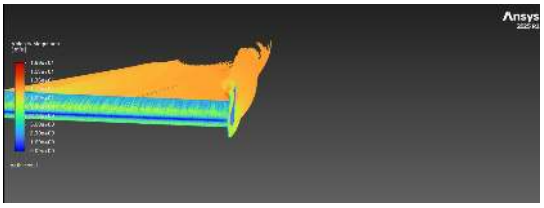

(a) Front view of the winglet with pathlines.

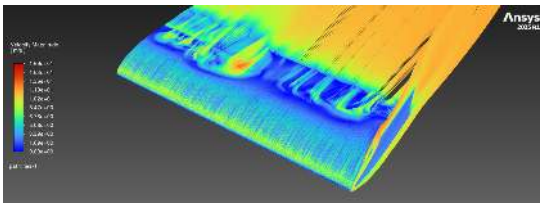

(b) Top view of the winglet with pathlines.

Fig. 36: Pathlines with the winglet.

From Fig. 37a, it can be clearly observed that the velocity field on the wing surface remains more uniform and well-structured up to the wingtip when winglets are present, compared to the configuration without winglets shown in Fig. 37b (red circle). This behavior indicates a reduction of the spanwise flow and a weakening of the wingtip vortices.

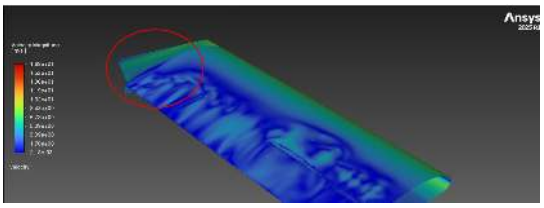

(a) Velocity contour plots with winglet

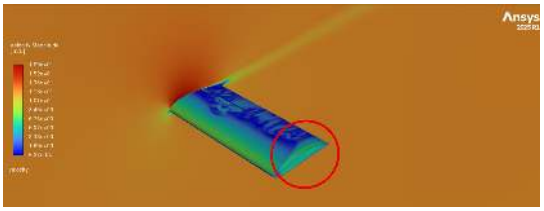

(b) Velocity contour plots without winglet

Fig. 37: Velocity contour plots.

Tip vortices lead to a non-uniform lift distribution. By mitigating the intensity of these vortices, winglets reduce the induced downwash and allow the local flow velocity and pressure fields to remain more coherent near the wingtip. As a result, the pressure distribution along the wing span becomes more homogeneous, approaching the ideal elliptical lift distribution, which is known to minimize induced drag. This improved spanwise pressure and lift distribution directly contributes to the observed increase in overall lift and aerodynamic efficiency.

3) Fuselage: Since the VTOL aircraft chassis consists of a single slender carbon rod with a square cross-section and does not include a conventional fuselage, lift-induced drag effects also manifest at the inner wing tips. In the absence of a fuselage, the pressure difference between the lower and upper wing surfaces promotes a spanwise flow near the wing root, leading to the formation of inner vortical flow structures.

To mitigate this effect, a fuselage-like fairing was introduced, which in practice consists of a thin red adhesive plastic film connecting the left and right wings. Rather than acting as a true fuselage, this element primarily serves as a separation between the upper low-pressure region and the lower high-pressure region, as illustrated in Fig. 38. By limiting the pressure-driven flow between these regions, this configuration reduces the formation of inner vortices and contributes to an improved lift distribution along the wing span.

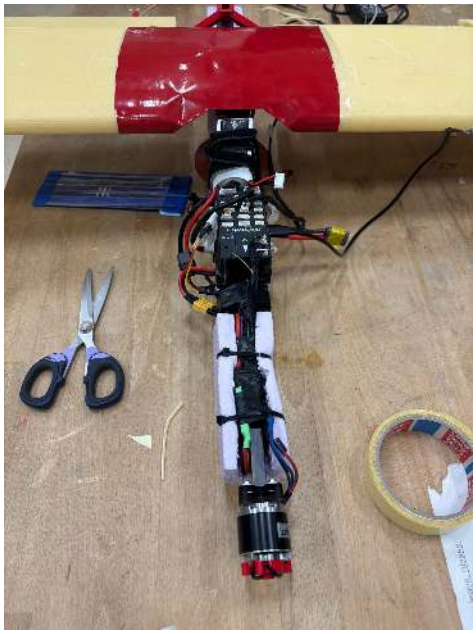

Fig. 38: Overview illustrating the thin adhesive red plastic film that plays the role of the fuselage.

D. Aerodynamic Stability

An aerodynamic stability analysis was conducted on the second iteration of the fixed-wings RC plane, shown in Fig. 39, using the software *Flow5*. This tool is specifically designed for preliminary aerodynamic analyses of lifting surfaces operating at low Reynolds numbers.

Fig. 39: Plane v2 prototype used for aerodynamic stability analysis.

Flow5 is based on potential flow theory and includes several inviscid aerodynamic methods, such as a non-linear Lifting-Line Theory formulation following NACA Report 1269, as well as Vortex Lattice and panel methods suitable for three-dimensional configurations. Wake effects can be modeled using either classical vortex representations or Lagrangian vortex particle methods. Although inviscid in nature, viscous effects are accounted for through coupling with two-dimensional viscous airfoil data generated using XFLR5. Owing to its low computational cost and its ability to capture stability characteristics, Flow5 is well suited for early-stage stability analyses.

1) Inertia of the Aircraft: To perform both static and dynamic stability analyses, knowledge of the aircraft center of mass is required. Fig. 40 illustrates the mass distribution of the aircraft and the resulting center of mass, which is indicated by the green circle in the figure.

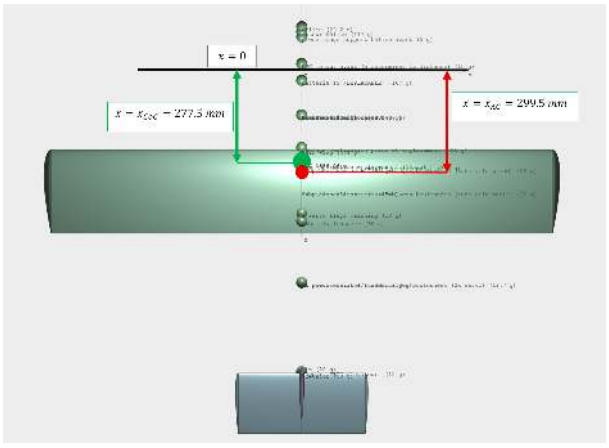

Fig. 40: Overview illustrating the masses repartition of the third iteration of our VTOL aircraft.

Due to issues encountered during fixed-wing flight, this iteration of the VTOL aircraft was specifically focused on improving maneuverability in airplane mode and therefore does not include the four propellers required for vertical takeoff and landing.

2) Static Stability [8]: A first and essential prerequisite for static longitudinal stability is that the aircraft center of mass must be located ahead of the aerodynamic center, which is typically situated at approximately one quarter of the chord length measured from the leading edge. It is important to note that the aerodynamic center should not be confused with the center of pressure. The aerodynamic center is defined as the point along the chord about which the aerodynamic pitching moment remains nearly constant with changes in angle of attack. In contrast, the center of pressure corresponds to the point of application of the resultant aerodynamic force and varies significantly with angle of attack. For stability analysis, the aerodynamic center is therefore the more appropriate reference. In the present configuration, the aerodynamic center of the aircraft is located at $x_{\mathrm{AC}} = 299.5\,\mathrm{mm}$, shown in Fig. 40 (red circle), while the center of mass is located at $x_{\mathrm{CoG}} = 277.5\,\mathrm{mm}$. This relative positioning satisfies the static stability requirement.

Static longitudinal stability can be assessed by examining the variation of the pitching moment coefficient C_m as a function of the angle of attack. As shown in Fig. 41, the blue curve represents the pitching moment coefficient of the aircraft. For static stability, it is essential that this curve passes through the origin and exhibits a negative slope. A negative slope indicates that an increase in angle of attack produces a restoring pitching moment. Indeed, if a gust increases the angle of attack by pitching the nose upward, the resulting negative pitching moment generates a nose-down tendency, thereby stabilizing the aircraft.

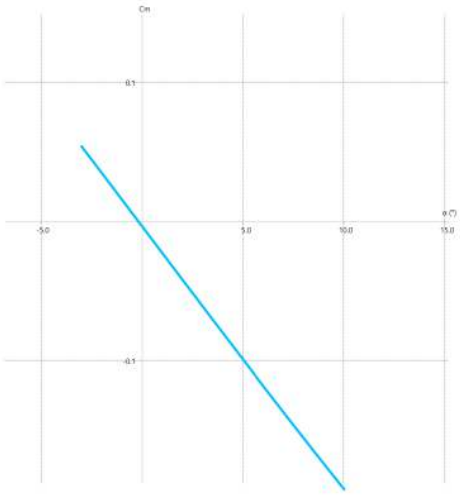

Fig. 41: Pitching moment curve in function of the angle of attack.

Another important aspect of static stability can be inferred from the relationship between the pitching moment coefficient and the lift coefficient. For a statically stable and trimmed aircraft, it is required that the lift coefficient corresponding to zero pitching moment has to be positive, as shown in Fig. 42. This condition ensures that, in steady level flight, the aircraft produces sufficient lift while remaining in equilibrium. According to classical aerodynamic theory, this also implies that the aircraft can be trimmed at a positive lift coefficient without relying on unstable configurations, which is a fundamental requirement for practical and controllable flight.

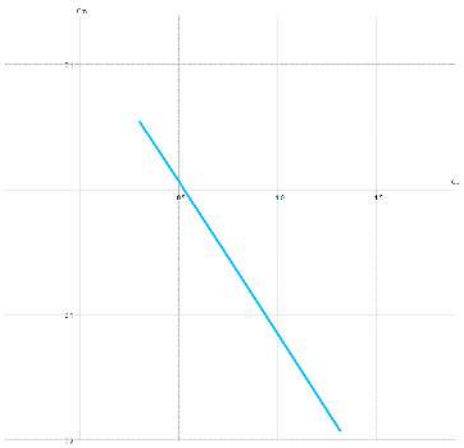

Fig. 42: Pitching moment curve in function of the lift coefficient.

A commonly used parameter to characterize the static stability of an aircraft is the static margin (SM). The SM of the VTOL aircraft can now be evaluated to further assess its longitudinal static stability. Indeed, as illustrated in Fig. 43, a positive static margin implies that the aircraft naturally generates a restoring pitching moment in response to a disturbance, thereby stabilizing the aircraft. A static margin equal to zero corresponds to a neutrally stable configuration, for which no restoring or destabilizing pitching moment is generated following a disturbance. In this case, the aircraft neither returns to nor diverges from its initial equilibrium state. Finally, a negative static margin indicates a statically unstable configuration, where a disturbance in angle of attack produces a pitching moment that amplifies the disturbance rather than counteracting it, leading to a divergence from the equilibrium condition.

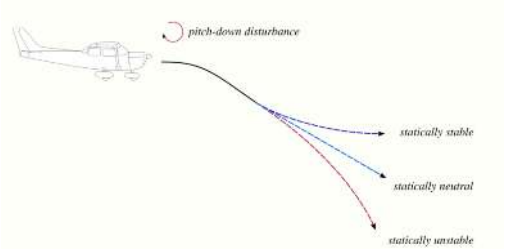

Fig. 43: Three different static responses due to a pitch-down disturbance [9].

The SM value is given by the following equation:

$$\text{Static margin} = \frac{x_{\text{neutral point}} - x_{\text{CoG}}}{c} = \frac{360 - 277.5}{250} = 0.33, \tag{19}$$

The resulting static margin is therefore equal to 0.33. This positive value indicates that the aircraft is statically stable in the longitudinal direction. Moreover, a static margin of this magnitude provides a good compromise between stability and controllability, ensuring stable flight behavior without excessively penalizing maneuverability.

The neutral point corresponds to the hypothetical longitudinal position of the aircraft center of mass for which the pitching moment coefficient remains independent of the angle of attack. In other words, at the neutral point, the aircraft exhibits neutral static stability. As shown in Fig. 44, the neutral point pitching moment curve is represented by the green curve, while the blue curve corresponds to the actual center of mass pitching moment curve of the aircraft.

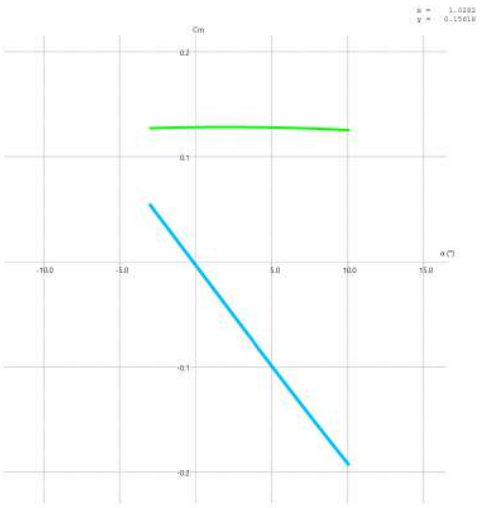

Fig. 44: Constant pitching moment curve corresponding to a CoG at the neutral point in function of the angle of attack.

3) Dynamic Stability [8]: The dynamic stability of the VTOL aircraft is analyzed by examining the characteristic longitudinal and lateral–directional dynamic modes. In the longitudinal axis, the aircraft motion is governed by the *short-period* and *phugoid* modes, which describe the fast and slow responses in pitch, angle of attack and airspeed. In the lateral–directional axis, the dynamic behavior is characterized by the *roll subsidence*, *Dutch roll* and *spiral* modes, which involve combinations of roll and yaw motions. The stability and damping characteristics of these five modes provide a comprehensive assessment of the dynamic response of the aircraft following a disturbance. An example of this behavior is illustrated in Fig. 45, which shows the aircraft response following a pitch disturbance for different damping conditions of the first longitudinal dynamic mode, namely the short-period mode. Depending on the level of damping, the aircraft may exhibit a dynamically unstable, dynamically damped, or overdamped response, while remaining statically stable.

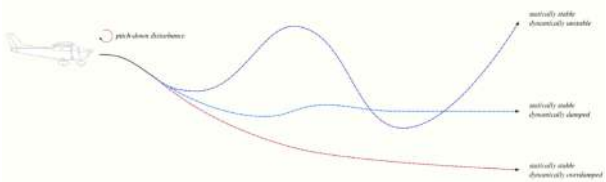

Fig. 45: Different damping conditions of the first longitudinal dynamic mode called ”short-period mode” [9].

Fig. 46 presents the aircraft response corresponding to the first longitudinal dynamic mode, namely the *short-period*

mode. This mode is characterized by a fast, heavily damped response dominated by variations in angle of attack and pitch rate, with only limited influence on the aircraft forward velocity. The *top-left* plot shows the fluctuation of the longitudinal velocity component u. The rapid decay toward zero indicates that variations in forward speed are minimal and quickly damped, confirming that the short-period mode is not primarily associated with energy exchange but rather with attitude dynamics. The *top-right* plot presents the vertical velocity component w, which exhibits a brief transient followed by a rapid convergence toward equilibrium. This behavior reflects the short-lived vertical motion induced by a pitching disturbance and is typical of the short-period response. The *bottom-left* plot shows the pitch rate q, which initially reaches a large magnitude and then decays rapidly without sustained oscillations. This confirms that the short-period mode is dominated by pitching dynamics and is strongly damped, leading to a fast stabilization of the rotational motion. Finally, the *bottom-right* plot presents the pitch angle θ, which returns quickly to its equilibrium value after a short transient. The absence of long-period oscillations indicates a well-damped short-period mode, which is essential for good handling qualities and pitch controllability of the aircraft.

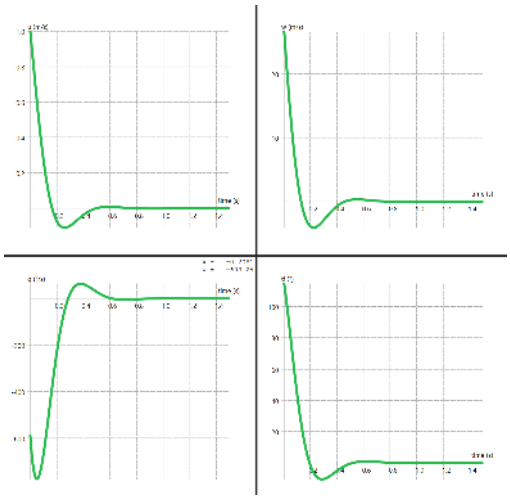

Fig. 46: The first longitudinal–directional dynamic mode : the short-period mode.

Fig. 47 presents the aircraft response corresponding to the second longitudinal dynamic mode, namely the phugoid mode. This mode is characterized by slow, lightly damped oscillations involving an exchange between kinetic and potential energy, and it predominantly affects the aircraft forward speed u and pitch attitude. The *top-left* plot shows the fluctuation of the longitudinal velocity component u. A long-period oscillatory behavior with very slow amplitude decay can be observed over the full time span up to $500\,\mathrm{s}$. This indicates that variations in forward speed are only weakly damped, which is a defining characteristic of the phugoid mode. The *top-right* plot presents the vertical velocity component w, which also exhibits slow oscillations with gradually decreasing amplitude. These oscillations reflect the vertical motion associated with the conversion between altitude and airspeed during the phugoid motion. The *bottom-left* plot shows the pitch rate q, which oscillates with relatively small amplitudes compared to the short-period mode and decays very slowly. This confirms that rotational dynamics are not dominant in the phugoid mode, which is instead governed by translational motion. Finally, the *bottom-right* plot presents the pitch angle θ, which undergoes long-period oscillations with a slow decay toward equilibrium. The presence of weakly damped oscillations over several hundred seconds confirms that the phugoid mode is dynamically stable but lightly damped, a behavior commonly observed in aircraft with positive static stability.

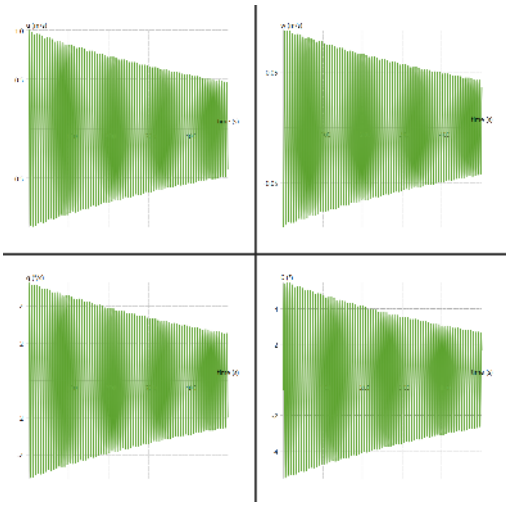

Fig. 47: The second longitudinal–directional dynamic mode : the phugoid mode.

Fig. 48 illustrates the aircraft response corresponding to the first lateral–directional dynamic mode, namely the *roll subsidence mode*. This mode is characterized by a fast, non-oscillatory decay dominated by roll motion and is typically the most heavily damped lateral mode. The *top-left* plot shows the lateral velocity component v, which rapidly decays to zero without oscillations. This behavior indicates that any initial sideslip disturbance is quickly attenuated and does not contribute significantly to the dynamics of this mode. The *top-right* plot presents the roll rate p, which exhibits a very large initial magnitude followed by a rapid exponential decay. This confirms that the roll subsidence mode is primarily governed by roll dynamics and is strongly damped, leading to a fast stabilization of the roll motion. The *bottom-left* plot shows the yaw rate r, which also decays rapidly toward zero. Although yaw is not the dominant motion in this mode, its fast decay reflects the strong damping present in the lateral–directional dynamics. Finally, the *bottom-right* plot shows the bank angle ϕ, which converges monotonically toward a steady value without oscillations. This non-oscillatory behavior is a hallmark of the roll subsidence mode and confirms that the aircraft quickly returns to a stable rolling equilibrium following a disturbance.

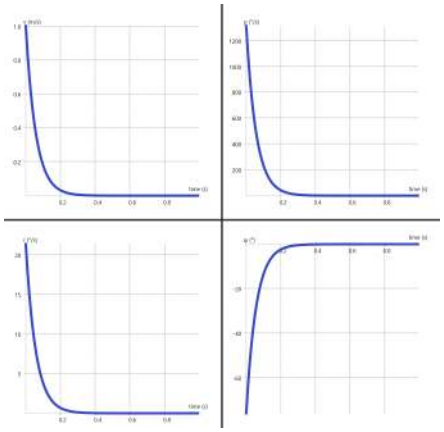

Fig. 48: The first lateral–directional dynamic mode : the roll subsidence mode.

Fig. 49 shows the response of the aircraft corresponding to the second lateral–directional dynamic mode, namely the *Dutch roll mode*. This mode is characterized by an oscillatory motion involving a strong coupling between yaw and roll dynamics. The *top-left* plot presents the lateral velocity component v, which exhibits an oscillatory behavior with a decreasing amplitude over time. This indicates that sideslip disturbances induce oscillations that are progressively damped, a typical feature of the Dutch roll mode. The *top-right* plot shows the roll rate p, which also displays oscillations that decay with time. Although roll motion is not dominant (see plot scale) in this mode, its coupling with yaw leads to noticeable roll-rate oscillations synchronized with the lateral motion. The *bottom-left* plot illustrates the yaw rate r, which shows pronounced oscillations with relatively larger initial amplitudes compared to the roll rate. This confirms that the Dutch roll mode is primarily yaw-dominated, with roll acting as a secondary coupled response. Finally, the *bottom-right* plot shows the bank angle ϕ, which oscillates around zero with a decreasing amplitude and eventually converges to the equilibrium position. The presence of damped oscillations in all lateral–directional variables indicates that the Dutch roll mode is dynamically stable for the considered configuration.

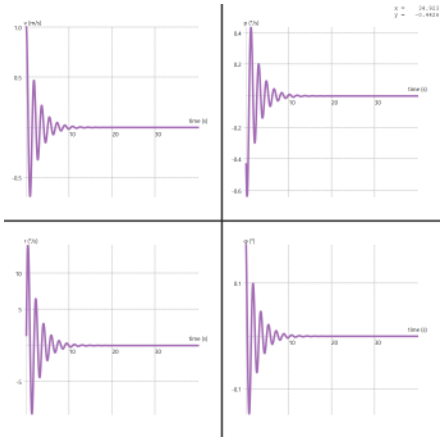

Fig. 49: The second lateral–directional dynamic mode : the Dutch roll mode.

Fig. 50 presents the response of the VTOL aircraft for the third lateral–directional dynamic mode, namely *the spiral mode*. This mode is characterized by a slow, non-oscillatory response involving coupled roll and yaw motions. The *top-left* plot shows the lateral velocity component v, corresponding to motion along the axis perpendicular to the aircraft forward direction. The monotonic decay of v indicates that lateral sideslip disturbances are gradually damped over time. The *top-right* plot shows the roll rate p, which initially exhibits a finite value and then slowly converges toward zero. This behavior is typical of the spiral mode, where roll dynamics evolve slowly rather than oscillating. The *bottom-left* plot presents the yaw rate r, which also decreases progressively toward zero, confirming that yaw motion is damped in the long term. The coupled decay of roll and yaw rates is a characteristic feature of the spiral mode. Finally, the *bottom-right* plot shows the bank angle ϕ (roll angle). The gradual decay of ϕ toward zero indicates that the aircraft eventually returns to wings-level flight. The absence of divergence confirms that the spiral mode is stable, although weakly damped, which is consistent with classical aircraft dynamic behavior.

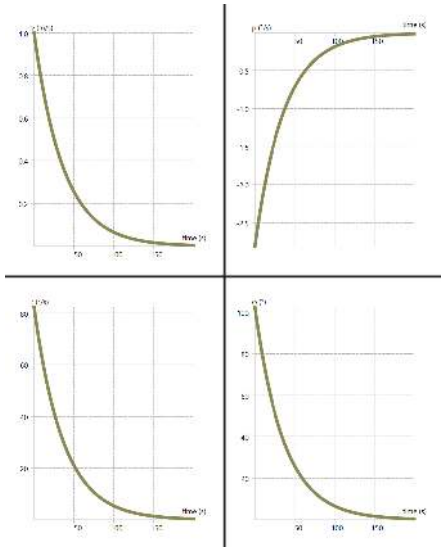

Fig. 50: The third lateral–directional dynamic mode : the spiral mode.

V. Experimental Results and Limitations

A. Evolution of the Prototypes and Test Flights

1) Plane v1 – Geometry and Handling Validation: The objective of the first fixed-wing prototype (see Fig. 51) was to validate the overall aircraft geometry at full scale and to gain initial experience with the handling and control of an aircraft of comparable size to the final design. Particular attention was given to control surface sizing, flap configuration, component placement, and general stability characteristics.

This prototype was constructed from expanded polystyrene foam, shaped using hot-wire cutting techniques. The propulsion system was intentionally simple, with the motor mounted at the nose using elastic attachments, in order to minimize

structural complexity and facilitate rapid modifications. Despite its simplicity, the prototype exhibited stable and predictable flight behavior. Test flights confirmed adequate controllability and validated the chosen wing geometry and control surface layout, providing a reliable baseline for subsequent iterations.

Fig. 51: Plane v1 prototype.

2) Quadcopter v1 – Hover Mode and Electronics Validation: In parallel with the fixed-wing development, a dedicated quadcopter prototype was built to validate hover-mode operation and the electronic architecture (see Fig. 52). The airframe was based on a standard 7-inch FPV quadcopter frame, selected for its availability and robustness.

The primary objectives of this prototype were to verify correct operation of the electronic components (ESCs, motors, Pixhawk flight controller), validate wiring and power distribution, and become familiar with QGroundControl for configuration and tuning. Initial tests were conducted on a secured indoor test bench equipped with a gimbal and linear slider, allowing safe evaluation of stabilization and control logic. After successful bench testing and the addition of landing supports, outdoor flight tests were performed, initially with a safety tether. These flights confirmed stable hover performance and provided confidence in the electronics and software setup.

Fig. 52: Quadcopter v1 prototype on the test bench.

3) VTOL v1 – Structural Integration and Mass Sensitivity: This prototype already included the structural framework based on a full-scale round aluminum tube skeleton, as illustrated in Fig. 53.

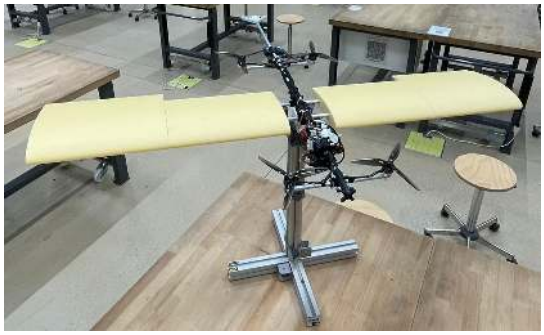

Fig. 53: VTOL v1 prototype.

It was equipped with two XPS wings, resulting in a total wingspan of 1.2 m. It was known that these wings were significantly lighter than the retractable wings planned for the final configuration; therefore, the drone was ballasted to compensate for this mass difference. In addition, the VTOL chassis was based on a structural framework composed of round aluminum tubes. This introduced significant alignment issues for the four propellers in quadcopter mode. Indeed, due to the circular cross-section of the tubes, the motor mounts exhibited a tendency to rotate and slip under load, leading to misalignment between the front and rear propellers. In practice, this resulted in the front propellers being tilted in one direction while the rear propellers were tilted in the opposite direction, which proved to be highly detrimental to stability in quadcopter mode. Nevertheless, the drone was able to perform several flights in quadcopter mode, executing yaw maneuvers and remaining steerable in all directions, despite significant vibrations. Two trials were conducted in fixed-wing mode, both resulting in crashes immediately upon launch. An excessively steep launch angle leading to a rapid stall, combined with insufficient thrust, are the most likely causes of these failures.

Fig. 54: VTOL v1 prototype successful hover flight.

4) Plane v2 – Power, Control Authority, and Structural Improvements: The third fixed-wing prototype, illustrated in Fig. 55 was designed to address the limitations identified during VTOL v1 testing which were mainly related to the

transition from round-section tubes to square-section tubes to address the connection and alignment issues encountered in the previous version. Regarding this drone, a decision was made to proceed initially with a fixed-wing configuration, excluding the quadcopter components. The objective is to validate flight performance in fixed-wing mode first; the quadcopter system will be integrated only once a robust and stable platform has been established. During the first flight test of the plane v2 prototype, an issue occurred at the aircraft launch. The aircraft was unable to adequately correct its pitch attitude, most likely due to an underpowered elevator. As a result, it reached a high angle of attack, leading to an aerodynamic stall, as illustrated in Fig. 56. The aircraft subsequently crashed.

Fig. 55: Plane v2 prototype.

(a) (b)

Fig. 56: Takeoff stall most likely caused by an undersized elevator.

For the second flight test, modifications were implemented on the tail assembly, including changes to the horizontal stabilizer and the elevator, as observable in Fig. 57b. A more powerful motor, providing approximately 200W, was also installed. These modifications resulted in one of the most successful flights of the project, resulting in a controlled and successful landing.

(a) (b)

Fig. 57: Successful flight achieved with the plane v2 prototype.

Finally, in order to match the estimated mass of the retractable wings, the drone was ballasted with approximately 300 g. Unfortunately, the flight conducted after this additional mass was introduced encountered the same launch issue as illustrated in Fig. 56. The propulsion system, which was not sufficiently powerful, combined with an elevator that remained slightly undersized, is believed to have been the primary cause of this failure. In addition, the wings had been originally dimensioned for a lower overall mass. As a consequence of the increased takeoff weight, the available lift margin was reduced, which further contributed to the observed launch difficulties. To address these problems, several key modifications were implemented in the plane V2 prototype, including an increase in propulsion power from 200 W to 380 W, an increase in wingspan from 1.2 m to 1.5 m to improve lift and a significant enlargement of the elevator and rudder surfaces to enhance control authority These successive design evolutions culminated in the prototype presented in Fig. 58.

Fig. 58: V2 prototype with 380W engine and greater control surface

To enhance flight stability, the wing placement was modified from a low-wing configuration (see Fig. 58) to a high-wing configuration mounted above the fuselage (see Fig. 59). Furthermore, this geometric change allowed for a reduction in the size of the landing skids, thereby decreasing both the system's mass and aerodynamic drag.

However, during the subsequent flight tests, severe elevator oscillations were observed following the implementation of these new upgrades, mainly the installation of a new front

motor and the excessive enlargement of the elevator surface. These oscillations appeared shortly after takeoff (see Fig. 59) and ultimately led to structural failure of the empennage and the loss of the aircraft. Although a definitive identification cannot be made without dedicated aeroelastic measurements, the observed behavior is highly characteristic of control-surface flutter.

(a) Elevator exhibiting a critical upward oscillation amplitude

(b) Elevator exhibiting a critical downward oscillation amplitude

Fig. 59: Overview of oscillatory behavior potentially associated with an aeroelastic flutter mechanism.

Flutter is an aeroelastic instability resulting from the coupling between unsteady aerodynamic loads, structural elasticity, and inertial effects. Beyond a critical flight speed, this coupling can lead to self-excited oscillations whose amplitude grows rapidly, often without prior warning. In the present case, the phenomenon appeared only after several seconds of flight, which is consistent with flutter being primarily speed-dependent rather than directly related to the takeoff phase.

Several design aspects of the tail assembly likely contributed to this instability. First, the elevator geometry appears oversized relative to the horizontal stabilizer, as illustrated in Fig. 60, leading to a large aerodynamic moment arm about the hinge line. Indeed, its size is more than two times the size of the horizontal stabilizer (fixed part). Such a configuration significantly increases the unsteady aerodynamic forces acting on the control surface. Moreover, the elevator is not mass-balanced, as most of its mass is located aft of the hinge line, resulting in a rearward center of gravity. This configuration is known to be particularly unfavorable, since the combined effect of inertia and aerodynamic loading can form an unstable oscillatory system.

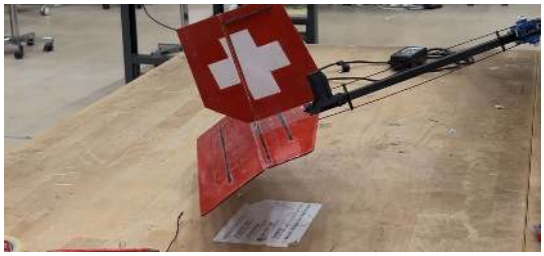

Fig. 60: Empennage configuration of the VTOL aircraft.

Second, the structural flexibility of the empennage plays a critical role. The tail is manufactured from balsa wood, reinforced with carbon rods, and the elevator hinge is realized using basic adhesive tape. While lightweight, this construction results in limited torsional stiffness and a compliant hinge, both of which are known to significantly reduce the flutter speed. Flutter is especially prone to occur in flexible control surfaces with soft hinges, as structural deformation feeds back into the aerodynamic loading.

Finally, any mechanical free play or compliance in the control system (including servo flexibility, long pushrods or any backlash in the transmission system from the servo to the elevator) can further amplify oscillations. At the high frequencies associated with flutter, the servo is unable to provide effective damping and may instead unintentionally sustain the oscillatory motion.

Although the exact origin of the observed oscillations cannot be conclusively attributed to flutter, the combination of an oversized and unbalanced elevator, low structural stiffness and a compliant hinge provides a plausible explanation for the instability encountered. To mitigate the risk of flutter in future iterations, several corrective actions are recommended: reducing the elevator chord to less than approximately 30–35% of the horizontal stabilizer chord, introducing mass balancing ahead of the hinge line, significantly increasing the torsional stiffness of the empennage and replacing the flexible tape hinge with a rigid mechanical hinge. Together, these measures would increase the flutter speed and improve the overall aeroelastic robustness of the aircraft.

In response to this issue, the chassis of the aircraft was upgraded from aluminum to carbon fiber tubes. This modification was implemented to increase structural stiffness while simultaneously reducing the overall weight of the system.

Although these improvements led to the onset of elevator oscillations, it was observed that during the few seconds preceding their appearance, the aircraft exhibited stable behavior and generated sufficient lift to support the additional ballast introduced to match the mass of the retractable wings. Unfortunately, further flight tests revealed persistent vibration-related issues that adversely affected sensor measurements and overall flight stability. These observations directly motivated both the vibration mitigation strategies and the control tuning discussed in the *Software* section, as well as the introduction of TPU interfaces and damping layers to reduce vibrations transmitted to the Pixhawk. In addition, they led to a redesign of the elevator, which was now shortened in order to reduce its dynamic response and mitigate the onset of oscillations.

5) Final Prototype – Retractable Wings VTOL Proof of Concept: The final prototype (Fig. 1) integrates the retractable wing system, including the scissor-based deployment mechanism, dedicated actuation electronics, and the hover propulsion units required for VTOL operation. The primary objective of this prototype was to serve as a proof of concept for the mechanical deployment system and its integration with the electronic and control architecture.

We initially evaluated the UAV performance using a static, non-retractable wing configuration, with an approximate total mass of 1.6 kg. Flight tests confirmed that this configuration capable of stable flight and successfully navigating through obstacles where the aperture was narrower than the UAV's full wingspan (see Fig. 61). While the platform demonstrated good maneuverability on all three axes, it was prone to significant vibrations. Furthermore, a noticeable instability in the roll axis was observed, primarily due to the reduced lateral distance between the left and right motor pairs.

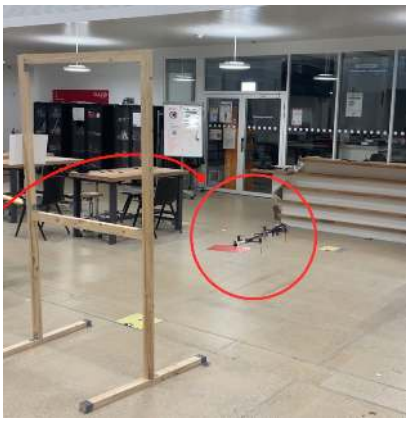

Fig. 61: Flight test obstacle: The drone is successfully traversing a window sized opening whose shape is smaller than the UAV's full wingspan.

The addition of the retractable wings, deployment mechanism, and quadcopter propulsion resulted in a total mass of approximately 2.6 kg. At this stage, it became evident that the initial motor sizing, which was performed early in the project based on lower mass estimates, was insufficient to safely lift and stabilize the vehicle in hover mode. As a result, free-flight VTOL tests were not conducted.

Nevertheless, extensive ground tests were performed to validate wing deployment and retraction using the RC transmitter, as well as to verify the reliability of the deployment mechanism and associated electronics. The prototype was also evaluated using the WindShape setup to qualitatively assess aerodynamic behavior. Due to remaining uncertainties regarding wing lift efficiency and hover thrust margins, outdoor fixed-wing flight tests were not attempted with the final configuration.

B. WindShape Experiments

1) Assessment of Flap Effectiveness on the Retractable Wing: A series of experiments was conducted in the windshape of the Laboratory of Intelligent Systems (LIS) on the EPFL campus, using retractable wings with a wingspan of 600 mm, as shown in Fig. 62a and an upstream flow velocity of approximately 12 m/s. The objective of these tests was to assess the effectiveness of the flaps integrated into the retractable wing configuration.

To this end, three experimental runs were performed: one with the flap in its neutral position, one with the flap deflected upward (flap-up) and one with the flap deflected downward (flap-down), as illustrated in Fig. 62b.

(a) Flap in its neutral position.

(b) Flap deflected downward (flap-down).

Fig. 62: Experimental results at the wind-shape of the lift comparison.

As shown in Fig. 63, the flap-up configuration generates a downforce, demonstrating the aerodynamic effectiveness of the flap. In this study, the downforce corresponds to positive values of the measured force. Conversely, the flap-down configuration leads to a significant increase in lift compared to the neutral case. This behavior is consistent with classical aerodynamic theory, where downward flap deflection increases the effective camber of the airfoil, thereby enhancing circulation and lift. These results are therefore reassuring with respect to the correct mechanical and aerodynamic functioning of the flaps.

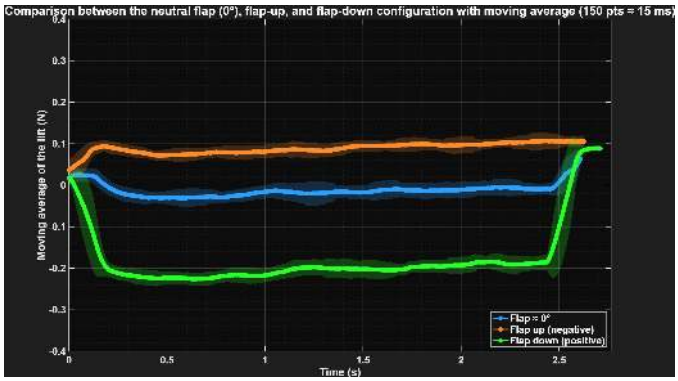

Fig. 63: Experimental results at the WindShape of the flap effectiveness.

2) Lift Evaluation of the Final Version of the Retractable Wings : Another test conducted at the LIS wind-shape was carried out to evaluate the lift generated by the final PET-CF/carbon fiber retractable wing configuration with a wingspan of $1500\ mm$, as illustrated in Fig. 64.

Fig. 64: Final version of our retractable wings.

This test consisted in comparing the retractable wings with XPS wings with the same wingspan, shown in Fig. 65, representing an ideal reference configuration, in order to quantify the lift loss induced by the retractable design with an upstream velocity of $10\ m/s$.

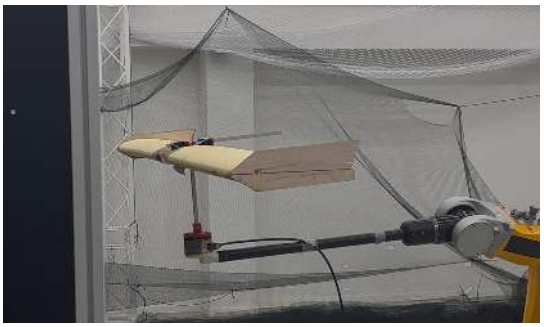

Fig. 65: XPS version of our wings.

As illustrated in Fig. 66a, the comparison was performed over a range of angles of attack from $0°$ to $8°$. At first glance, the CFD results obtained using the Simplified Model of the Retractable Wing (green curve) appear to overestimate the lift forces measured experimentally, including those obtained with the XPS reference wing.

However, this discrepancy must be interpreted with caution, as the experimental measurements for both the XPS wing and the retractable wing were conducted at a free-stream velocity of $10\,\mathrm{m\,s^{-1}}$, whereas the CFD simulations were performed at the cruise velocity of $12\,\mathrm{m\,s^{-1}}$. Since lift scales approximately with the square of the free-stream velocity, the higher velocity used in the numerical simulations naturally leads to increased lift values. Indeed, the free-stream velocity used in the CFD simulations ($12\,\mathrm{m\,s^{-1}}$) is 1.2 times larger than the velocity used during the wind-shape experiments ($10\,\mathrm{m\,s^{-1}}$), the lift is expected to scale approximately with the square of the velocity, i.e. by a factor of $1.2^2 \approx 1.44$.

Applying this scaling to the experimental results obtained with the retractable wing leads to the following estimated lift values at $12\,\mathrm{m\,s^{-1}}$: at $\alpha = 0°$, the lift would increase from $2.9\,\mathrm{N}$ to approximately $4.2\,\mathrm{N}$, compared to $4.9\,\mathrm{N}$ predicted by CFD; at $\alpha = 4°$, the lift would increase from $7.15\,\mathrm{N}$ to approximately $10.3\,\mathrm{N}$, compared to $12.45\,\mathrm{N}$ predicted by CFD; and at $\alpha = 8°$, the lift would increase from $11.51\,\mathrm{N}$ to approximately $16.6\,\mathrm{N}$, compared to $19.3\,\mathrm{N}$ predicted by CFD.

A similar scaling applied to the XPS reference wing yields estimated lift values of approximately $6.0\,\mathrm{N}$, $12.5\,\mathrm{N}$, and $20.0\,\mathrm{N}$ at $\alpha = 0°$, $4°$, and $8°$, respectively, which are in very close agreement with the corresponding CFD predictions.

This comparison shows that, once the difference in free-stream velocity is taken into account, the simplified three-dimensional CFD model provides a reasonably accurate estimation of the experimental lift magnitude of the retractable and XPS wing. While the model does not achieve exact quantitative agreement, it captures the correct order of magnitude and overall lift trend, making it a valuable tool for preliminary aerodynamic assessment of the retractable wing. It is, however, important to note that the three-dimensional CFD model features a wingspan of $1250\,\mathrm{mm}$, whereas the XPS and retractable wing experimental models have a larger wingspan of $1500\,\mathrm{mm}$. This difference in aspect ratio directly affects the lift generated by the wing and may partly explain the good agreement observed between the theoretical predictions and the experimental measurements.

Furthermore, the lift generated by the retractable wing remains relatively close to that of the XPS reference wing, which is encouraging given that XPS wings are known to exhibit good aerodynamic performance in practice. Indeed, the relative errors shown in Fig. 66b remain below 18% for all angles of attack, except at $0°$, where larger discrepancies are observed. These results therefore suggest that the final retractable wing design exhibits promising aerodynamic behavior and a strong potential for successful flight performance, despite a modest loss of lift attributable to the absence of winglets on the retractable wings.

Nevertheless, further improvements could still be achieved by developing a more accurate three-dimensional CAD model, in particular by representing more realistically the openings present around the retractable wing cells (identified as being responsible for part of the observed loss of lift) and by refining the mesh in the regions directly in contact with the wing.

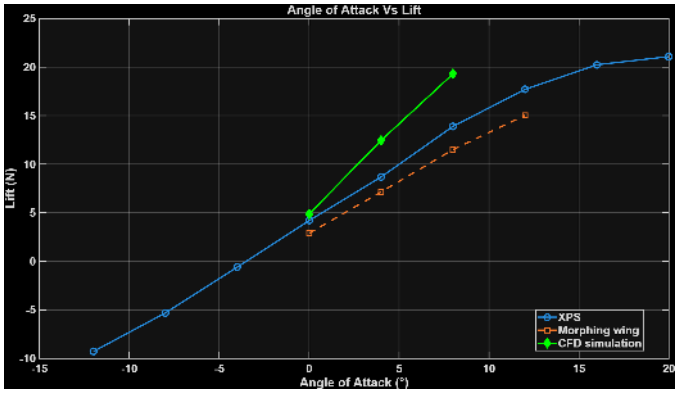

(a) Lift as a function of the angle of attack for the XPS wing and the retractable wing measured at a free-stream velocity of $10\,\mathrm{m\,s^{-1}}$, compared with CFD simulation results obtained at a free-stream velocity of $12\,\mathrm{m\,s^{-1}}$.

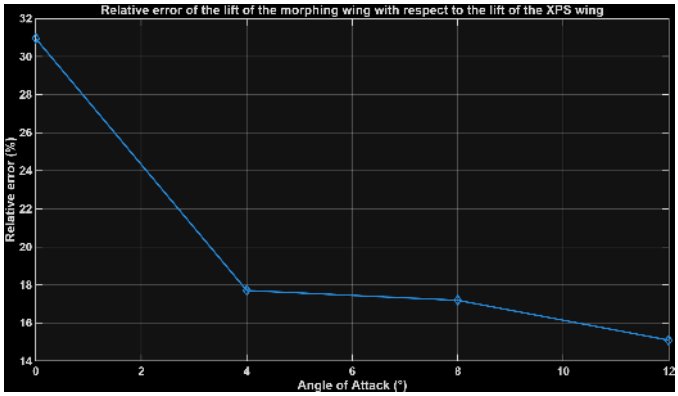

(b) Relative error of the lift of the retractable wing with respect to the lift of the XPS wing.

Fig. 66: Experimental results at the WindShape of the lift comparison.

C. Potential Improvements

Several design improvements and architectural evolutions could be considered in future iterations of the prototype.

First, the four landing and take-off support poles could be removed. Instead, the drone could directly take off from and land on the folded wings themselves. This would require local structural reinforcement of the wing edges to withstand ground contact loads. In addition to reducing mass and mechanical complexity, the removal of these poles would also decrease parasitic drag during fixed-wing flight, thereby improving overall aerodynamic efficiency.

Currently, when the wings are fully deployed, a residual gap remains between the extrados and intrados at the leading edge of certain wing cells. This geometric discontinuity degrades the aerodynamic continuity of the airfoil and results in suboptimal lift generation. Future work should focus on improving the closure and alignment of the leading-edge geometry in order to eliminate these gaps and enhance lift performance.

The concept of a compact drone with retractable wings could be further extended by introducing retractability to the tail assembly. Since the tail does not contribute to stability or control during quadcopter mode, its length could be reduced in this configuration. This could be achieved by implementing a telescopic main frame section downstream of the wing mechanism, allowing the tail to deploy simultaneously with the wings during transition to fixed-wing flight.

To reduce the total number of propulsion units, the dedicated forward propulsion motor could be eliminated. Instead, the quadcopter motors could be reconfigured to provide forward thrust. This could be realized either by tilting the four motors by 90° once a sufficient altitude is reached, or by tilting only two motor pairs. In such a configuration, vertical take-off would rely on conventional multirotor operation, while forward flight would be achieved using the same propulsion units.

Further aerodynamic optimization could be achieved by redesigning the front motor mounts to eliminate the drag induced by the current transverse support bars. In the proposed design, the structural beam perpendicular to the airflow would be integrated internally within the wing root. The motors would be mounted on longitudinal booms extending forward from the leading edge, connected via an internal elbow. This configuration aligns the exposed support structure parallel to the freestream and allows the deployable wing cells to retract over the internal beam, significantly reducing parasitic drag.

With the same objective of drag reduction, the second transversal bar supporting the rear quadcopter motors could also be removed. The corresponding motors could instead be integrated into the tail assembly, which would require a complete redesign of the empennage, potentially adopting a V-tail configuration. Such a modification would significantly alter the control architecture, requiring a different allocation and tuning of elevator and rudder functions.

Finally, the two rear quadcopter motors could be replaced by a tricopter configuration using a single central rear propeller positioned between the wing and the tail. Yaw control could be achieved using either a tilting mechanism or counter-rotating propellers. This solution would further reduce mass and mechanical complexity while maintaining full attitude control authority.

From an integration standpoint, no dedicated landing gear is required for the prototype. When the wings are folded, they act as stable support points on the ground, allowing safe takeoff, landing, and ground handling without additional structural elements.

VI. Conclusion

This project presented the design, development, and partial experimental validation of a novel VTOL drone architecture combining multirotor hovering capabilities with the aerodynamic efficiency of fixed-wing flight. While the system integrates multiple mechanical, electronic, and control subsystems, the retractable wing mechanism remains the core and most innovative contribution of this work.

The proposed wing architecture is based on a scissor-type retractable mechanism using rigid wing cells, enabling a high retraction ratio while preserving a continuous aerodynamic profile in the deployed configuration. Unlike conventional folding or telescopic wing concepts, this solution avoids nested

structures and geometric discontinuities, allowing the wings to compact efficiently within a reduced span while maintaining structural stiffness and aerodynamic continuity.

The wing concept was supported by an extensive aerodynamic study. Numerical simulations were conducted to evaluate the aerodynamic performance of the deployed wing configuration, including lift generation, drag behavior, and stability characteristics. These simulations confirmed that the selected wing geometry and airfoil provide sufficient aerodynamic performance for efficient forward flight, while remaining compatible with the mechanical constraints imposed by the retractable architecture. The aerodynamic results directly informed the design of the wing cells and validated the feasibility of the fixed-wing flight mode.

However, despite numerical analyses, the complete VTOL flight sequence could not be achieved. During final integration and testing, issues related to system tuning, mass distribution, and control authority prevented a stable and reliable execution of the full VTOL operation. As a result, a complete transition from vertical takeoff to sustained fixed-wing flight was not successfully demonstrated within the scope and timeframe of this project. These limitations highlight the complexity inherent to hybrid VTOL platforms, where strong coupling exists between aerodynamics, structural design, propulsion, and control.

Nevertheless, the experimental results confirm the technical feasibility and robustness of the retractable wing concept itself, independently of the full VTOL performance. The challenges encountered at the system level provide valuable insight and clearly identify directions for future improvements.

Future work will focus on refining the control architecture, improving mass distribution and propulsion sizing, and conducting incremental flight testing to progressively validate hover, transition, and fixed-wing flight phases. With these improvements, the proposed retractable wing architecture has strong potential to be fully demonstrated in a complete VTOL flight scenario.

In conclusion, this project demonstrates that a scissor-based retractable rigid wing, supported by aerodynamic simulations and experimental prototyping, is a promising solution for compact VTOL drones, even though a full VTOL demonstration was not achieved. The work provides a solid foundation for future developments and contributes a novel wing architecture to the field of compact and morphing aerial vehicles.

Acknowledgment

The authors would like to express their gratitude to Simon Jaeger (LIS Laboratory) for his supervision of this project, his guidance during weekly meetings, and his critical assistance during the WindShape sessions and flight tests.

We gratefully acknowledge the financial support provided by the EPFL XPlore Association. We specifically thank Giovanni Ranieri (EPFL Xplore) for his oversight of resource management, his role in facilitating collaboration within the association, and his valuable feedback on the project's progress.

Finally, we extend our thanks to Julius Wanner (LIS Laboratory) for his support during the WindShape experiments and data extraction, as well as Martin Mayer (EPFL Sola) for his technical insights and assistance regarding the eCalc and Flow5 software simulations.

References

[1] Z. Min, V. K. Kien, and L. J. Richard, "Aircraft morphing wing concepts with radical geometry change," *The IES Journal Part A: Civil & Structural Engineering*, vol. 3, no. 3, pp. 188–195, 2010.

[2] "Design and aerodynamic analysis of the morphing waverider with rotating telescopic wing for wide-speed-range flight," *Aerospace Science and Technology*, 2025.

[3] X. Y. Zhao and J. Hu, "Research on aerodynamic characteristics of morphing aircraft with a telescopic wing," in *Advanced Materials Research*, vol. 709, 2013, pp. 257–261.

[4] Wikipedia, "Finesse (aérodynamique)," 2024, accessed: 28/12/2025. [Online]. Available: https://fr.wikipedia.org/wiki/Finesse_(arodynamique)

[5] Wikipedia contributors, "Naca airfoil — Wikipedia, the free encyclopedia," 2024, [Online; accessed 30-December-2025]. [Online]. Available: https://en.wikipedia.org/wiki/NACA_airfoil

[6] National Advisory Committee for Aeronautics, "Report 824—summary of airfoil data," 1945, [Online; accessed 30-December-2025]. [Online]. Available: https://ntrs.nasa.gov/citations/19930090976

[7] J. D. Anderson, *Fundamentals of Aerodynamics*, 6th ed. New York, USA: McGraw-Hill Education, 2017.

[8] Techwinder, "Youtube channel tutorials," 2016, [Online; accessed 31-December-2025]. [Online]. Available: https://www.youtube.com/@techwinder/playlists

[9] Encyclopedia, "Static stability of aircraft," 2022, [Online; accessed 30-December-2025]. [Online]. Available: https://encyclopedia.pub/entry/30410

[10] É. Boujo, "Numerical flow simulation," Course notes, ME-474, 2025.

[11] K. A. J. Mulleners, "Aerodynamics," Course notes, ME-445, 2025.

[12] André, "Flow5 documentation," 2024, [Online; accessed 30-December-2025]. [Online]. Available: https://flow5.tech/docs/flow5_doc/flow5_doc.html

APPENDIX

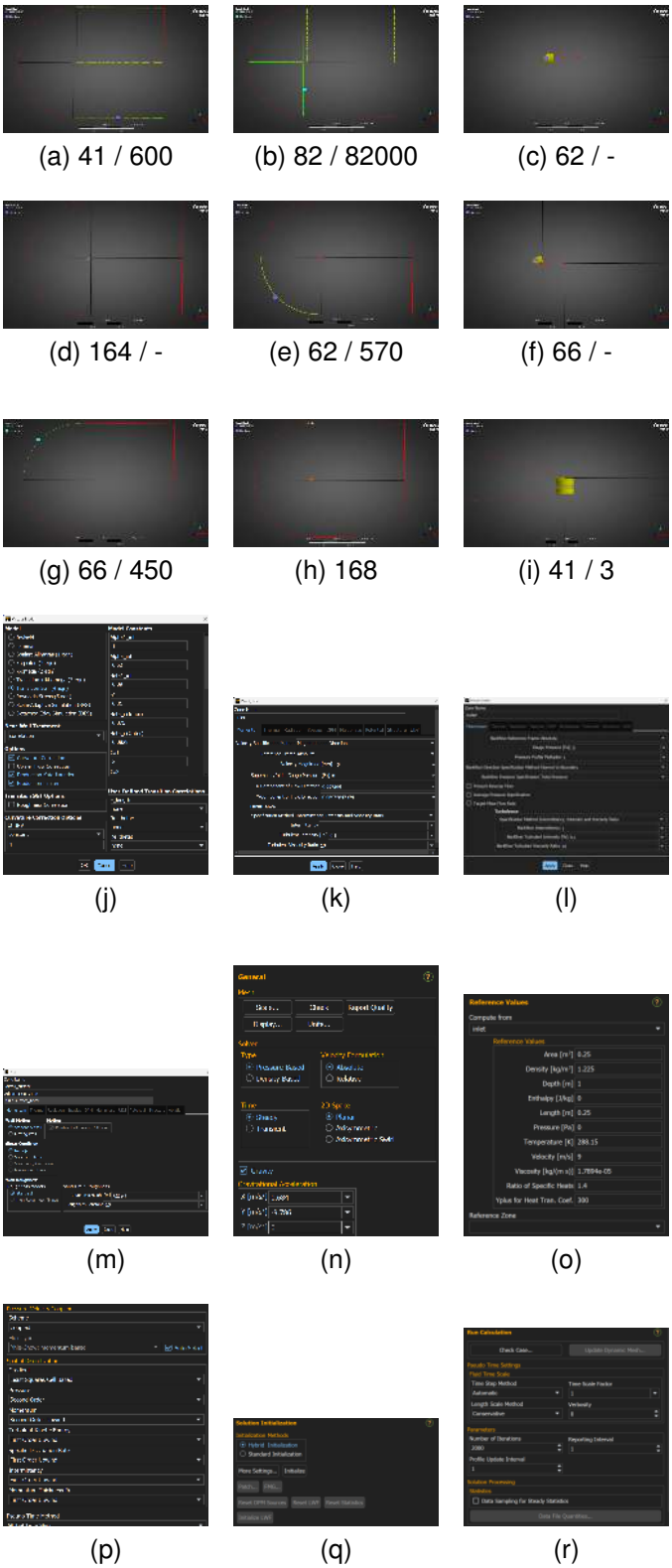

(a) 41 / 600 (b) 82 / 82000 (c) 62 / -

(d) 164 / - (e) 62 / 570 (f) 66 / -

(g) 66 / 450 (h) 168 (i) 41 / 3

(j) (k) (l)

(m) (n) (o)

(p) (q) (r)

Fig. 67: Settings of the mesh edge sizing and Fluent solver for the 2D simulations.

Here are the settings used for the *2D VTOL Wing Dimensioning* simulations, performed with an airfoil of chord length 250 mm. For the *2D Mesh Validation* simulations, only the geometry proportions relative to the airfoil chord were varied and also the spatial discretization scheme was set to second order for all parameters. The edge sizing figures from (a) to (i) report : the number of divisions (X) and the applied bias factor (Y) in the following format : X / Y.

Here are the settings used for the *3D Simplified Model of the Morphing Wing with Winglets* simulations, performed with a wing of chord length 250 mm and a wingspan of 625 mm. For the *3D Mesh Validation* simulations, only the geometry propor-

tions relative to the wing chord were varied. For the *3D VTOL Wing Dimensioning* and *3D Simplified Model of the Morphing Wing* simulations, the geometry, the mesh parameters all other numerical settings were kept identical. The figures related to the mesh from (a) to (g) (covering edge sizing, surface sizing, and the body of influence (BOI)) report the element size of the cells in millimeters.

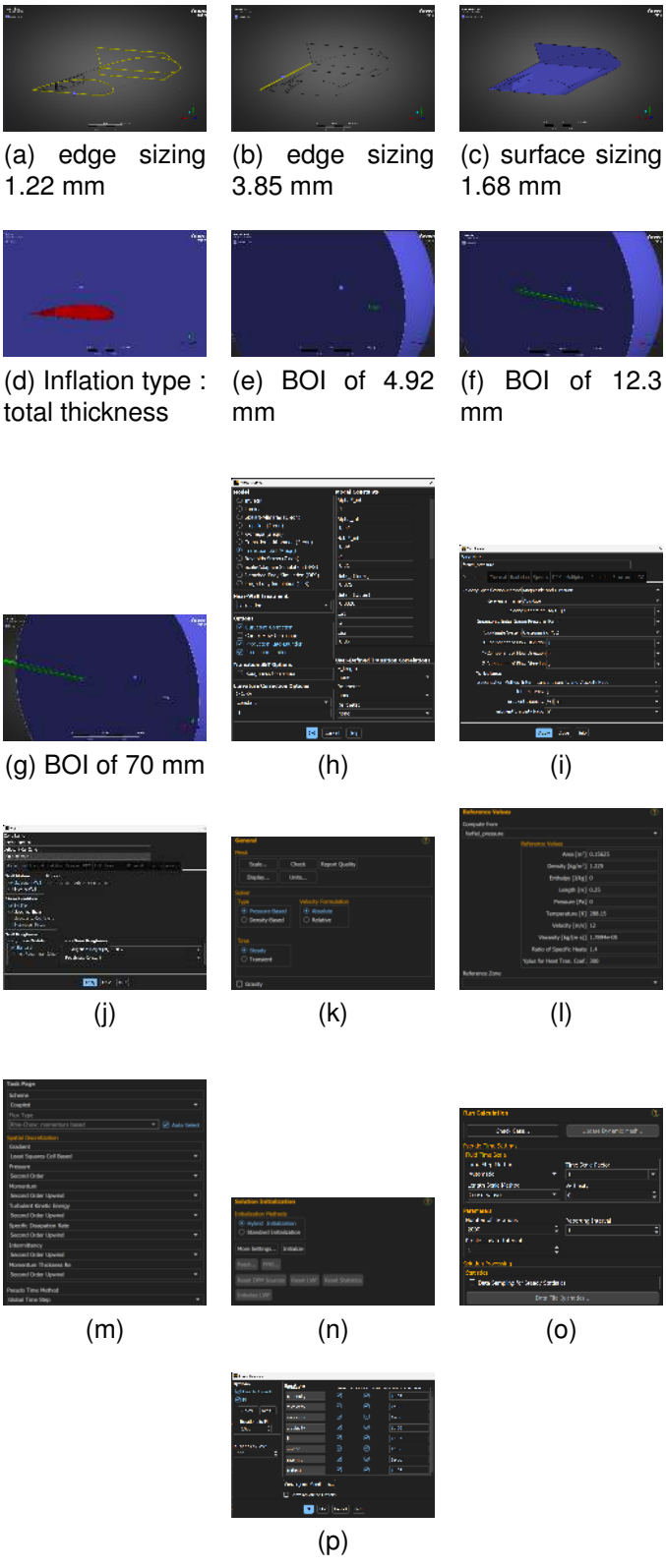

(a) edge sizing 1.22 mm (b) edge sizing 3.85 mm (c) surface sizing 1.68 mm

(d) Inflation type : total thickness (e) BOI of 4.92 mm (f) BOI of 12.3 mm

(g) BOI of 70 mm (h) (i)

(j) (k) (l)

(m) (n) (o)

(p)

Fig. 68: Settings of the mesh sizing and Fluent solver for the 3D simulations.